Numerical and experimental analysis of shallow turbulent flow over complex roughness beds

Numerical and Experimental Analysis of Shallow Turbulent Flow over Complex Roughness Beds

Yong Zhang, *State Key Laboratory of Hydroscience and Engineering, Tsinghua University, Beijing 100084, China*
Email: zhang.yong.sichuan@163.com

Matteo Rubinato, *Faculty of Engineering, Environment & Computing, School of Energy, Construction and Environment, Coventry University, Coventry, CV1 5FB, UK*
Email: *matteo.rubinato@coventry.ac.uk* *ORCiD orcid.org/0000-0002-8446-4448*

Ehsan Kazemi, *Department of Civil and Structural Engineering, The University of Sheffield, Sheffield S1 3JD, UK*
Email: e.kazemi@sheffield.ac.uk, ORCiD: orcid.org/0000-0002-1780-1846

Jaan H. Pu, *Faculty of Engineering and Informatics, University of Bradford, Bradford, BD7 1DP, UK*
Email: J.H.Pu1@bradford.ac.uk ORCiD: orcid.org/0000-0002-3944-8801

Yuefei Huang, *State Key Laboratory of Hydroscience and Engineering, Tsinghua University, Beijing 100084, China*
Email: yuefeihuang@tsinghua.edu.cn

Pengzhi Lin, *State Key Laboratory of Hydraulics and Mountain River Engineering, Sichuan University, Chengdu 610065, China*
Email: cvelinpz@scu.edu.cn (corresponding author)

ABSTRACT

A set of shallow-water equations (SWEs) based on a $\hat{k}-\hat{\varepsilon}$ Reynold stress model is established to simulate the turbulent flows over a complex roughness bed. The fundamental equations are discretized by the second-order finite-difference method (FDM), in which spatial and temporal discretization are conducted by staggered-grid and leap-frog schemes, respectively. The turbulent model in this study stems from the standard $\hat{k}-\hat{\varepsilon}$ model, but is enhanced by replacing the conventional vertical production with a more rigorous and precise generation derived from the energy spectrum and turbulence scales. To verify its effectiveness, the model is applied to

compute the turbulence in complex flow surroundings (including a rough bed) in an abrupt bend and in a natural waterway. The comparison of the model results against experimental data and other numerical results shows the robustness and accuracy of the present model in describing hydrodynamic characteristics, especially turbulence features on the complex roughness bottom.

***Keywords*:** Energy spectrum, Roughness bed, SWE model, Shallow flows, Turbulent flows

1 Introduction

Large and small turbulent swirling flows are often clearly observable when dealing with hydraulic structures in rivers and coastal areas and they are a key factor that influence the frequency and magnitude of natural processes such as the sediment transport, mixing of pollutants and/or riverbed deformation. Therefore, to better manage the rivers and design reliable hydraulic structures, it is fundamental to understand these features and facilitate their predictions. However, certain external factors (e.g. various and inconsistent boundary conditions) make the characterizations of turbulent flows very challenging. To the author's knowledge, there is not yet a fully accurate, time-convenient, or general numerical model to completely replicate the turbulent flows and their impacts over a natural roughness bed. Despite that, effective simulations of the turbulent flow for some specific scenarios have been made due to the rapid progress on the numerical modeling techniques and the computing powers.

The nature of turbulence is fundamentally three-dimensional (3D). Historically, 3D approaches on the turbulence modeling mainly included the Direct Numerical Simulation (DNS), Large-Eddy Simulation (LES), and Reynolds-Averaged Navier-Stokes (RANS) modeling [1-4]. Along the rivers and coastal regions, the flow domain is quite complex and spacious, and hence to characterize the flow structures it would be excessively time-consuming to apply any of these three approaches, which would require a large number of grid nodes in order to provide the accurate results [5]. The two-dimensional (2D) Shallow Water Equations (SWE) coupled with the benchmark turbulence closure model is much faster and enables the interpretation of turbulent characteristics using a smaller vertical length scale (z) as compared with the two horizontal ones (x *and* y) in those regions [6-9]. Furthermore, to obtain more accurate and repeatable results, it is also critical to select the appropriate coefficients in these turbulence closure equations.

2D shallow-turbulence flow models have been extensively developed over the last decades. Most of the available ones are based on the Boussinesq approximations. For example, the depth-averaged eddy viscosity model suggests that eddy viscosity is the simple product of the bed shear velocity and water depth [10] and the depth-averaged mixing length model accounts for the influence of vertical turbulence [11]. Rastogi and Rodi [12] established the 2D standard depth-averaged $\hat{k}-\hat{\varepsilon}$ turbulence model based on the 3D version described by Launder and Spalding [13]. To widen the range of practical applications, some coefficients in the model developed by Rastogi and Rodi were modified and new $\hat{k}-\hat{\varepsilon}$ models were introduced, as presented in the other studies [14-18]. The standard $\hat{k}-\hat{\varepsilon}$ model has been demonstrated to provide satisfactory results after numerous comparisons with the measured data [11,14] and it is also relatively simple to use and very fast. Despite this, more progresses have been made in this field and recently, Cea *et al.* [11] established a depth-averaged algebraic stress turbulence model (DASM) to solve a single transport equation for each Reynolds stress without requiring an isotropic assumption.

For the shallow turbulent flows on a roughness bed, the vertical velocity gradient distribution is the main source of turbulence. The accuracy of its depth-averaged process directly determines the numerical performance of the aforementioned $\hat{k}-\hat{\varepsilon}$ models. To date there is still area for improvement due to the fact that preliminary results of the standard $\hat{k}-\hat{\varepsilon}$ model only partially agree with the experimental data [12]. According to Rastogi and Rodi [12], this may be related to the bottom shear stress, via the friction velocity, under the assumption of similarity in the vertical velocity profiles. The depth-averaging process is a consideration only of the macroscopic effects of the bottom roughness on the turbulent generations. In the classic "cascade" theory of energy introduced by Richardson [19], the turbulent motion is a process of energy transfer among various scales including not only the macroscale, but also various microscales [2, 20, 21]. The contribution of these features should be rigorously and precisely replicated within turbulent closure models.

The turbulent structure of various scales based on the framework of energy cascade can be divided into the energy-containing, inertial, and dissipative regions, respectively. The kinetic energy, produced in the energy-containing region, is considered to be transferred by inertial forces to smaller scales until the energy is typically dissipated by the molecular viscosity [2]. The energy spectrum in the inertial region has a universal statistical form, i.e. the Kolmogorov -5/3 spectrum [22], and can be applied to larger or smaller wave numbers as the Reynolds number increases [8]. Nezu and Nakagawa [20] analogized the energy transfer processes to

open-channel flows and divided the whole water depth into the three regions: wall, intermediate, and free-surface zones. A universal log-law in the intermediate region was verified by the extensive experimental and numerical results and they confirmed this can be applied to a wider range of bed roughness and Reynolds numbers.

Taking into considerations all of these previous works and the new insights that have been provided, this study aims to improve the performance of the standard $\hat{k}-\hat{\varepsilon}$ model to characterise the generation of turbulent conditions at various scales over complex roughness beds. The numerical SWE model utilised in this work includes a second-order leap-frog finite-difference method (FDM) and it is built into a staggered-grid system. This model was initially developed by Cho [23] to calculate the evolution of the long waves and was further extended by Lin [24] to simulate the turbulent structures within an experimental zone. Lately this turbulence model has been widely used to compute the complex flows induced by irregular geometries and the results obtained have proven that it is a robust numerical technique [25-27]. In the present study, we emphasized the improvement of the model for application to the complex roughness beds.

The paper is organized as follows: *Section 2* presents the description of the mathematical and numerical shallow turbulence model considered for this study, clarifying various assumptions and hypothesis: the governing equations are presented in *Section 2.1*, then the vertical turbulent production is formulated in *Section 2.2* by incorporating the energy transfer information between various scales into P_{kV} and $P_{\varepsilon V}$ based on the two universal semi-theoretical formulas of Kolmogorov -5/3 scaling law and log-law. *Section 3* includes the validation of the numerical model against the experimental data collected on a flume, where varying roughness on the bed was tested with a complex sharp bend. Finally, to further demonstrate the potentials of the model, its performance was more vigorously examined in the transport of moraine along the Yangtze River under dry seasons, and the results are explained in *Section 4*. *Section 5* provides a brief summary and concluding remarks of the whole study.

2 Numerical Model

2.1 Governing equations

This section presents the governing equations and the boundary conditions utilised in this study.

2.1.1 Shallow-water equations

The time-dependent SWEs are the fundamental hydrodynamic equations described in this

section. By integrating the Reynolds Averaged Navier-Stokes (RANS) equations along the entire water depth and assuming the vertical flow to be nearly-uniform and pressure distributions to be hydrostatic, the SWEs can be given as follows [25-27]:

$$\frac{\partial H}{\partial t}+\frac{\partial P}{\partial x}+\frac{\partial Q}{\partial y}=0 \tag{1a}$$

$$\frac{\partial P}{\partial t}+\frac{\partial}{\partial x}\left(\frac{P^2}{H}\right)+\frac{\partial}{\partial y}\left(\frac{PQ}{H}\right)+gH\frac{\partial \eta}{\partial x}=\frac{1}{\rho}\frac{\partial\left(HT_{xx}\right)}{\partial x}+\frac{1}{\rho}\frac{\partial\left(HT_{yx}\right)}{\partial y}-\frac{f}{8H^2}\sqrt{P^2+Q^2}P-\frac{2}{3}\frac{\partial\left(H\hat{k}\right)}{\partial x} \tag{1b}$$

$$\frac{\partial Q}{\partial t}+\frac{\partial}{\partial x}\left(\frac{PQ}{H}\right)+\frac{\partial}{\partial y}\left(\frac{Q^2}{H}\right)+gH\frac{\partial \eta}{\partial y}=\frac{1}{\rho}\frac{\partial\left(HT_{xy}\right)}{\partial x}+\frac{1}{\rho}\frac{\partial\left(HT_{yy}\right)}{\partial y}-\frac{f}{8H^2}\sqrt{P^2+Q^2}Q-\frac{2}{3}\frac{\partial\left(H\hat{k}\right)}{\partial y} \tag{1c}$$

where $H\left(=\eta-z_b\right)$ is the water depth, in which η and z_b are the free surface and bed elevation, respectively (Fig. 1); $P\left(=HU\right)$ and $Q\left(=HV\right)$ are components of unit volume flux, in which $U\left(=\frac{1}{H}\int_{z_b}^{\eta}\langle u\rangle dz\right)$ and $V\left(=\frac{1}{H}\int_{z_b}^{\eta}\langle v\rangle dz\right)$ are the depth-averaged velocities in *x* and *y* directions, respectively; g is gravitational acceleration; ρ is fluid density; $\hat{k}\left(=\frac{1}{H}\int_{z_b}^{\eta}kdz\right)$ is the depth-averaged turbulent energy; T_{xx}, T_{yy}, T_{yx}, and T_{xy} are the depth-averaged effective stresses expressed as follows [25-26]:

$$T_{xx}=2\rho\frac{\nu+\hat{\nu}_t}{H}\frac{\partial P}{\partial x} \tag{2a}$$

$$T_{yy}=2\rho\frac{\nu+\hat{\nu}_t}{H}\frac{\partial Q}{\partial y} \tag{2b}$$

$$T_{yx}=T_{xy}=\rho\frac{\nu+\hat{\nu}_t}{H}\left(\frac{\partial P}{\partial y}+\frac{\partial Q}{\partial x}\right) \tag{2c}$$

where ν and $\hat{\nu}_t$ are the kinematic viscosity and the depth-averaged turbulent viscosity, respectively, as defined in Eq. (4).

f in Eq. (1) is the bed friction factor defined according to parameters for the smooth and rough beds previously obtained [26, 28], such as Chézy-Manning's and Altsul's formula:

$$f=\frac{8gm^2}{H^{1/3}} \tag{3a}$$

157 $$f = 0.1\left(1.46\frac{k_s}{R} + \frac{100}{\mathrm{Re}}\right)^{1/4} \quad (3$$

158 b)

159 where m is Manning's roughness coefficient; k_s is bed roughness height, which in this study
160 it is considered to be the median diameter of the bed material; R is the hydraulic radius (the
161 water depth, in this study); and *Re* is the Reynolds number.

162 *2.1.2 Depth-averaged $\hat{k}-\hat{\varepsilon}$ closure equations*

163 The depth-averaged velocity field in Eq. (1) can be solved when $\hat{\nu}_t$ is determined. The
164 specification of $\hat{\nu}_t$ is assumed to be mathematically analogous to the turbulent viscosity ν_t in
165 the standard $k-\varepsilon$ model [25], and can be expressed as follows:

166 $$\hat{\nu}_t = C_\mu \frac{\hat{k}^2}{\hat{\varepsilon}} \quad (4)$$

167 The transport equations $\hat{k}$ and $\hat{\varepsilon}$ can be then introduced, respectively, as follows:

168 $$\frac{\partial(H\hat{k})}{\partial t} + \frac{\partial(P\hat{k})}{\partial x} + \frac{\partial(Q\hat{k})}{\partial y} = H\hat{\nu}_t\left[2\left(\frac{\partial U}{\partial x}\right)^2 + 2\left(\frac{\partial V}{\partial y}\right)^2 + \left(\frac{\partial U}{\partial y} + \frac{\partial V}{\partial x}\right)^2\right] + P_{kV} + \frac{\partial}{\partial x}\left[\left(\nu + \frac{\hat{\nu}_t}{\sigma_k}\right)\frac{\partial(H\hat{k})}{\partial x}\right] + \frac{\partial}{\partial y}\left[\left(\nu + \frac{\hat{\nu}_t}{\sigma_k}\right)\frac{\partial(H\hat{k})}{\partial y}\right] - H\hat{\varepsilon} \quad (5a)$$

169 $$\frac{\partial(H\hat{\varepsilon})}{\partial t} + \frac{\partial(P\hat{\varepsilon})}{\partial x} + \frac{\partial(Q\hat{\varepsilon})}{\partial y} = C_{\varepsilon 1}\frac{\hat{\varepsilon}}{\hat{k}}H\hat{\nu}_t\left[2\left(\frac{\partial U}{\partial x}\right)^2 + 2\left(\frac{\partial V}{\partial y}\right)^2 + \left(\frac{\partial U}{\partial y} + \frac{\partial V}{\partial x}\right)^2\right] + P_{\varepsilon V} + \frac{\partial}{\partial x}\left[\left(\nu + \frac{\hat{\nu}_t}{\sigma_\varepsilon}\right)\frac{\partial(H\hat{\varepsilon})}{\partial x}\right] + \frac{\partial}{\partial y}\left[\left(\nu + \frac{\hat{\nu}_t}{\sigma_\varepsilon}\right)\frac{\partial(H\hat{\varepsilon})}{\partial y}\right] - C_{\varepsilon 2}H\frac{\hat{\varepsilon}^2}{\hat{k}} \quad (5b)$$

170 where $C_\mu, \sigma_k, \sigma_\varepsilon, C_{1\varepsilon}$ and $C_{2\varepsilon}$ are the empirical constants and their values, as recommended by
171 Launder and Spalding [13], are

172 $$C_\mu = 0.09, \sigma_k = 1.0, \sigma_\varepsilon = 1.3, C_{1\varepsilon} = 1.44, C_{2\varepsilon} = 1.92 \quad (6)$$

173 and, as suggested in [8], [12] and [13],

174 $$P_{kV} = \frac{n^2 g}{H^{\frac{1}{3}}}\left(U^2 + V^2\right)^{\frac{3}{2}} \quad (7a)$$

175 $$P_{\varepsilon V} = \frac{C_2 C_\mu n^{\frac{5}{2}} g^{\frac{5}{4}}\left(U^2 + V^2\right)^2}{H^{\frac{17}{12}}} \quad (7b)$$

2.2 Vertical turbulent production P_{kV} and $P_{\varepsilon V}$

P_{kV} and $P_{\varepsilon V}$ in Eq. (5) are the components generated by turbulence and can be defined as the tensor product of the horizontal Reynolds stress and vertical velocity gradient, respectively. In the context of homogeneous, open-channel turbulence, they represent all the turbulent energy produced. The corresponding expressions to calculate their magnitude were deduced by Rastogi and Rodi [12], although their derivations seemed to have overgeneralized the generation of vertical turbulent features.

According to the theory of cascade energy, which has been proven and validated against extensive experimental studies, the turbulent motion is a one-way energy transfer process from large scale eddies to smaller ones [2]. The theory can also be applied to the transfer of energy from the bottom of the river to the free surface [20]. To rigorously and precisely quantify the energy transfer across various scales, this study presents an additional model that estimates the generation of vertical turbulent features in a different manner, considering the interaction between points at different levels and the total energy spectrum. Bottom roughness elements markedly affect the amount of turbulence. Turbulence tends to be isotropy as the bed roughness and Reynolds numbers increase [2, 20,29]. Cea *et al.* [11] found a similar degree of accuracy between the $\hat{k}-\hat{\varepsilon}$ model, which is based on the concise isotropic hypothesis, and the DASM model, which includes complex model structures considering anisotropy. Based on this assumption, below are listed the steps selected to deduce the expressions of P_{kV} and $P_{\varepsilon V}$.

2.2.1 Mean velocity profiles

For a uniform and fully-developed turbulent flow in a wide open channel, the Reynolds equation in the *z*-direction (as derived from the Navier-Stokes equations) is reduced to:

$$\rho\nu\frac{d\langle u\rangle}{dz}-\rho\langle u'w'\rangle=\rho u_*^{\,2}\left(1-\frac{z}{H}\right) \tag{8}$$

where $\rho\nu\, d\langle u\rangle/dz$ is the viscous stress; $-\rho\langle u'w'\rangle$ is the Reynolds stress; $u_*\left(=\sqrt{\tau_b/\rho}\right)$ is the friction velocity, in which τ_b is the bed shear stress at $z=0$.

By considering the Prandtl's mixing-length hypothesis, ν can be expressed as the product of a velocity scale u^* and a length scale l_m, in which u^* is specified as $u^*=\left|\langle u'w'\rangle\right|^{1/2}$. From Eq. (8),

206 the following equation could be obtained:

207 $$\frac{d\langle u\rangle^+}{dz^+}=\frac{2\tau/\tau_b}{1+\sqrt{1+(4\tau/\tau_b)(l_m^+)^2}} \tag{9}$$

208 where $\langle u\rangle^+=\langle u\rangle/u_*$ and $z^+=zu_*/\nu_k$ are the dimensionless velocity and z-coordinate
209 normalized by the viscous length $\delta_\nu=\nu_k/u_*$, respectively; $l_m^+=l_m u_*/\nu_k$ is the dimensionless
210 mixing-length. If appropriate specification of l_m^+ over the whole depth can be obtained, Eq. (9)
211 can be easily integrated to yield the distribution of $\langle u\rangle$.
212
213 In various regions from $z=0$ to $z=\eta$, the effect of $\rho\nu\, d\langle u\rangle/dz$ and $-\rho\langle u'w'\rangle$ on the
214 velocity distribution is different. According to their contribution to the turbulent structure, the
215 vertical turbulence fields of $\langle u\rangle$ are divided into two regions: the inner region and the outer
216 region [20]. It is assumed that the viscous effect dominates the inner region (in general,
217 $z/H<(0.15-0.2)$), so the length scale can be denoted by δ_ν. The component τ/τ_w tends
218 towards unity and l_m^+ can be specified as $l_m^+=\kappa z^+$ in this region, so the solution to Eq. (9) (the
219 "log-law"), can be obtained as follows:

220 $$\langle u\rangle^+=\frac{1}{\kappa}\ln z^+ + A \tag{10}$$

221 where $\kappa=0.40-0.43$ and $B=5.2$ are the empirical constants [2, 30].
222
223 It is assumed that the viscous contribution in the outer region (generally, $z/H\geq(0.15-0.2)$) to
224 the turbulent structure is negligible, and that l_m^+ no longer depends on δ_ν. It is challenging to
225 solve Eq. (9) because there is no universal representation of l_m^+. The wake law provided by
226 Coles [31], is typically used to extend the log-law to the outer region. The profile of $\langle u\rangle$ in this
227 region can be approximated as follows:

228 $$\langle u\rangle^+=\frac{1}{\kappa}\ln z^+ + A+\frac{2\Pi}{\kappa}\sin^2\left(\frac{\pi z}{2H}\right) \tag{11}$$

229 where Π is Coles's wake-strength parameter. Π has been investigated in various studies where
230 its value has been suggested to be around 0.08-0.20. Π also shows no distinct value for flows
231 with different bed roughness conditions [32]. Considering the comparisons made by Pope [2]
232 and Nezu and Nakagawa [20], the profile of $\langle u\rangle$ can be effectively approximated by Eq. (11)
233 over the whole depth except in a small region near the bed. In the core region of closed-bed

234 flow (e.g., $z^+ < 26$), l_m^+ is strongly affected by the Reynolds number and bed roughness, so
235 $\langle u \rangle$ is likely to remain the complex profile. In this study, we considered the distribution of $\langle u \rangle$
236 in this region to be determined by using Eq. (11).

237 *2.2.2 Depth-averaged vertical production*

238 Based on Kolmogorov's scaling theory outlined at [22], the dissipation rate ε could be related
239 to $\|u'\|$ by using the macroscale of turbulence described in [20, 21] as follows:

240 $$\varepsilon = K \frac{\|u'\|^3}{L_x} \tag{12}$$

241 where $K = [2/(\pi C')]^{3/2} (L_x k_0)^{5/2}$ is a turbulent coefficient which is greatly influenced by the
242 Reynolds number, C' is a universal Kolmogorov constant, L_x is the longitudinal integral
243 macroscale, k_0 is macroscale of turbulence. Nakagawa et al. [33] suggested that $\|u'\|/u_*$ can be
244 approximated as the power function of z/H :

245 $$\frac{\|u'\|}{u_*} = \left[\frac{B_N}{\kappa K} \left(1 - \frac{z}{H} \right) \right]^{1/3} \left(\frac{z}{H} \right)^{-1/6} \tag{13}$$

246 Further, under an assumption of isotropy, Nezu and Nakagawa [20] found that the correlation
247 coefficients of turbulence intensities are nearly constant as long as z^+ is sufficiently large. This
248 can be approximately represented by:

249 $$\|w'\|/\|u'\| = C_1, \|v'\|/\|u'\| = C_2 \tag{14}$$

250 where C_1 and C_2 are empirical constants.

251

252 For stationary and homogeneous turbulence, the turbulent production $P_k \left(= -\langle u'w' \rangle \partial \langle u \rangle / \partial z \right)$ is
253 balanced approximately by the sum of the turbulent diffusion $D_k \left(= (d/dz) \left[(\nu/\sigma_k)(dk/dz) \right] \right)$
254 and dissipation ε independently of the molecular diffusion. In the inertial subrange, energy
255 transfer is the only significant process; there is no energy production or dissipation. Thus,
256 $P_k \approx \varepsilon$. The dynamic equilibrium of turbulent energy can then be expressed as follows:

257 $$\nu \frac{dk}{dz} = \text{const.} \tag{15}$$

258 in which $\nu \left(= C_\mu k^2 / \varepsilon \right)$ is the turbulent viscosity. Substituting Eq. (12) into ν (where L_x is of
259 the same order as H) and making use of Eq. (14) (where u' is of the order of u_*) yields the

following approximation of ν:

$$\nu \approx \frac{1}{k} H u_*^3 \tag{16}$$

Substituting Eq. (16) into Eq. (15) with the integral from 0 to z yields the distribution of k:

$$\frac{k}{u_*^2} = D \exp\left(-2C_k \frac{z}{H} \right) \tag{17}$$

where D and C_k are the constants. Applying Eqs. (14) and (17) provides the profiles of u', v', and w':

$$\frac{\|u'\|}{u_*} = D_u \exp\left(-C_k \frac{z}{H} \right) \tag{18a}$$

$$\frac{\|v'\|}{u_*} = D_v \exp\left(-C_k \frac{z}{H} \right) \tag{18b}$$

$$\frac{\|w'\|}{u_*} = D_w \exp\left(-C_k \frac{z}{H} \right) \tag{18c}$$

where D_u, D_v, D_w, and C_k are the empirical constants; their values are 2.30, 1.27, 1.63, and 1.0, respectively [20].

By closely examining the turbulence intensities presented by Nezu and Nakagawa [20], we found close agreement between Eq. (18) results and the experimental values throughout the whole depth apart from a thin layer near the bed. Surprisingly, any deviation between them gradually decreased as Re and k_s^+ ($= k_s u_* / \nu_k$) increased. To some extent, Eq. (18) is successful in displaying the vertical distribution of turbulence intensity. Integrating Eq. (18) with the given empirical constants allows the depth-averaged turbulent energy $\hat{k}$ to be obtained:

$$\hat{k} = 2.07 u_*^2 \tag{19}$$

The constant used in Eq. (19) has been found by combining D_u, D_v, and D_w at Eqs. (18a) – (18c), suggested in Nezu and Nakagawa [20]. The formulation of k is described in Eq. (37). According to the theory of cascade energy, at the end of the sequence of processes, the dissipation of turbulent energy is accomplished primarily by molecular viscosity. In other words, the energy of open-channel flows is predominantly dissipated in the free surface region. Observed ε values in this region are less accurate due to the constraints of free-surface fluctuations. In the comparison made by Nakagawa et al. [33], it is very difficult to obtain a universal formula for ε. In this study, we used ν as a replacement for ε to determine P_{kV} and $P_{\varepsilon V}$.

$$\nu = \frac{\kappa\left(1-z/H\right)Hu_*}{\left(H/z\right)+\pi\Pi\sin\left(\pi z/H\right)} \tag{20}$$

Eq. (20) is found from substituting Coles' law at Eq. (11) into Eq. (8). By integrating Eq. (20) from the bed to free surface, we obtained the depth-averaged turbulent viscosity $\hat{\nu}_t$ as follows:

$$\hat{\nu}_t = 0.06Hu_* \tag{21}$$

The constant in Eq. (21) comes from depth-averaging Eq. (20) from bed to free-surface, using described values of κ and Π in section 2.2.1. In stationary and homogeneous flows, P_{kV} and $P_{\varepsilon V}$ in the $\hat{k}-\hat{\varepsilon}$ transport equations are balanced only by their dissipation terms $\hat{\varepsilon}H$ and $C_{2\varepsilon}\hat{\varepsilon}^2H/\hat{k}$, respectively. P_{kV} and $P_{\varepsilon V}$ can be obtained by rearranging Eq. (5) and combining Eqs. (4), (19) and (21):

$$P_{kV} = 71.42C_\mu u_*^3 \tag{22a}$$

$$P_{\varepsilon V} = 2464.16C_\mu^2 C_{2\varepsilon}\frac{u_*^4}{H} \tag{22b}$$

where $u_* = \sqrt{f\left(U^2+V^2\right)/8}$. These Eqs. (22a) and (22b) have been derived from the standard $\hat{k}-\hat{\varepsilon}$ formulations of P_{kV} and P_{eV} terms as showing at Eqs. (7a) and (7b).

2.3 Numerical implementation

In this study, we discretized the fundamental equations using the explicit leap-frog FDM which has second-order accuracy in both time and space [25-26]. As plotted in Fig. 2, all of the vectors ($P, Q, U,$ and V) were evaluated at the faces of the grid; all of the scalars ($H, \eta, z_b, \hat{k},$ and $\hat{\varepsilon}$) were defined at the center of the grid. The defined location of the normal stresses (e.g., T_{xx} and T_{yy}) is the same as the scalar; the shear stresses (e.g., T_{xy} and T_{yx}) were calculated as shown in the right-top corner of the grid.

2.3.1 Continuity equation

According to the spatial staggered grid system and the temporal leap-frog scheme, the continuity equation is explicitly discretized as follows:

$$H_{i,j}^{n+1/2} = H_{i,j}^{n-1/2} - \frac{\Delta t}{\Delta x_i}\left(P_{i+1/2,j}^n - P_{i-1/2,j}^n\right) - \frac{\Delta t}{\Delta y_j}\left(Q_{i,j+1/2}^n - Q_{i,j-1/2}^n\right) \tag{23}$$

2.3.2 Momentum equations

Without loss of generality, only the discretized form of *x*-momentum equation is presented here in detail:

316
$$
\begin{aligned}
P_{i+1/2,j}^{n+1} = & \frac{1-\dfrac{f\Delta t}{16\left(H_{i+1/2,j}^{n}\right)^2}\left[\left(P_{i+1/2,j}^{n}\right)^2+\left(Q_{i+1/2,j}^{n}\right)^2\right]^{1/2}}{1+\dfrac{f\Delta t}{16\left(H_{i+1/2,j}^{n}\right)^2}\left[\left(P_{i+1/2,j}^{n}\right)^2+\left(Q_{i+1/2,j}^{n}\right)^2\right]^{1/2}}P_{i+1/2,j}^{n} \\
& -\frac{\Delta t}{1+\dfrac{f\Delta t}{16\left(H_{i+1/2,j}^{n}\right)^2}\left[\left(P_{i+1/2,j}^{n}\right)^2+\left(Q_{i+1/2,j}^{n}\right)^2\right]^{1/2}}\left\{\left[\frac{\partial}{\partial x}\left(\frac{P^2}{H}\right)\right]_{i+1/2,j}^{n}+\left[\frac{\partial}{\partial y}\left(\frac{PQ}{H}\right)\right]_{i+1/2,j}^{n}\right\} \\
& -\frac{g\Delta t}{\left\{1+\dfrac{f\Delta t}{16\left(H_{i+1/2,j}^{n}\right)^2}\left[\left(P_{i+1/2,j}^{n}\right)^2+\left(Q_{i+1/2,j}^{n}\right)^2\right]^{1/2}\right\}\Delta x_{i+1/2}}H_{i+1/2,j}^{n+1/2}\left(\eta_{i+1,j}^{n+1/2}-\eta_{i,j}^{n+1/2}\right) \\
& +\frac{\Delta t/\rho}{1+\dfrac{f\Delta t}{16\left(H_{i+1/2,j}^{n}\right)^2}\left[\left(P_{i+1/2,j}^{n}\right)^2+\left(Q_{i+1/2,j}^{n}\right)^2\right]^{1/2}}\left[\frac{\partial\left(HT_{xx}\right)}{\partial x}+\frac{\partial\left(HT_{yx}\right)}{\partial y}\right]_{i+1/2,j}^{n}
\end{aligned}
\tag{24}
$$

317 where the convection terms are respectively discretized as follows by applying the upwind
318 scheme:

319
$$
\left[\frac{\partial}{\partial x}\left(\frac{P^2}{H}\right)\right]_{i+1/2,j}^{n}=\begin{cases}\dfrac{\dfrac{\left(P_{i+1/2,j}^{n}\right)^2}{H_{i+1/2,j}^{n}}-\dfrac{\left(P_{i-1/2,j}^{n}\right)^2}{H_{i-1/2,j}^{n}}}{\Delta x_i} & if \quad P_{i+1/2,j}^{n}>0 \\ \dfrac{\dfrac{\left(P_{i+3/2,j}^{n}\right)^2}{H_{i+3/2,j}^{n}}-\dfrac{\left(P_{i-1/2,j}^{n}\right)^2}{H_{i-1/2,j}^{n}}}{\Delta x_i+\Delta x_{i+1}} & if \quad P_{i+1/2,j}^{n}=0 \\ \dfrac{\dfrac{\left(P_{i+3/2,j}^{n}\right)^2}{H_{i+3/2,j}^{n}}-\dfrac{\left(P_{i+1/2,j}^{n}\right)^2}{H_{i+1/2,j}^{n}}}{\Delta x_{i+1}} & if \quad P_{i+1/2,j}^{n}<0\end{cases}
\tag{25a}
$$

320
$$
\left[\frac{\partial}{\partial y}\left(\frac{PQ}{H}\right)\right]_{i+1/2,j}^{n}=\begin{cases}\dfrac{\dfrac{\left(PQ\right)_{i+1/2,j}^{n}}{H_{i+1/2,j}^{n}}-\dfrac{\left(PQ\right)_{i+1/2,j-1}^{n}}{H_{i+1/2,j-1}^{n}}}{\Delta y_{j-1/2}} & if \quad Q_{i+1/2,j}^{n}>0 \\ \dfrac{\dfrac{\left(PQ\right)_{i+1/2,j+1}^{n}}{H_{i+1/2,j+1}^{n}}-\dfrac{\left(PQ\right)_{i+1/2,j-1}^{n}}{H_{i+1/2,j-1}^{n}}}{\Delta y_{j-1/2}+\Delta y_{j+1/2}} & if \quad Q_{i+1/2,j}^{n}=0 \\ \dfrac{\dfrac{\left(PQ\right)_{i+1/2,j+1}^{n}}{H_{i+1/2,j+1}^{n}}-\dfrac{\left(PQ\right)_{i+1/2,j}^{n}}{H_{i+1/2,j}^{n}}}{\Delta y_{j+1/2}} & if \quad Q_{i+1/2,j}^{n}<0\end{cases}
\tag{25b}
$$

321 *2.3.3 Turbulent transport equations*

322 The $\hat{\varepsilon}-$ and $\hat{k}-$equations are respectively discretized by applying a semi-implicit scheme:

$$\hat{\varepsilon}_{i,j}^{n+1/2}=\frac{\frac{\left(H\hat{\varepsilon}\right)_{i,j}^{n-1/2}}{\Delta t}-F\hat{\varepsilon}X-F\hat{\varepsilon}Y+VIS\hat{\varepsilon}X+VIS\hat{\varepsilon}Y+C_{1\varepsilon}\frac{\hat{\varepsilon}_{i,j}^{n-1/2}}{\hat{k}_{i,j}^{n-1/2}}\left(P_h\right)_{i,j}^{n+1/2}+\left(P_{\varepsilon V}\right)_{i,j}^{n+1/2}}{\frac{H_{i,j}^{n+1/2}}{\Delta t}+C_{2\varepsilon}\frac{\hat{\varepsilon}_{i,j}^{n-1/2}}{\hat{k}_{i,j}^{n-1/2}}H_{i,j}^{n-1/2}} \tag{26a}$$

$$\hat{k}_{i,j}^{n+1/2}=\frac{\frac{\left(H\hat{k}\right)_{i,j}^{n-1/2}}{\Delta t}-F\hat{k}X-F\hat{k}Y+VIS\hat{k}X+VIS\hat{k}Y+\left(P_h\right)_{i,j}^{n+1/2}+\left(P_{kV}\right)_{i,j}^{n+1/2}}{\frac{H_{i,j}^{n+1/2}}{\Delta t}+C_{\mu}\frac{\hat{\varepsilon}_{i,j}^{n-1/2}}{\left(\hat{\nu}_t\right)_{i,j}^{n-1/2}}H_{i,j}^{n-1/2}} \tag{26b}$$

Similarly, the upwind scheme can be used to discretize the convective term $F\hat{\varepsilon}X$ (the differences of $F\hat{\varepsilon}Y$, $F\hat{k}X$, and $F\hat{k}Y$ are similar to $F\hat{\varepsilon}X$) as follows:

$$\left[F\hat{\varepsilon}X\right]_{i,j}^{n-1/2}=\left[\frac{\partial\left(P\hat{\varepsilon}\right)}{\partial x}\right]_{i,j}^{n-1/2}=\begin{cases}\dfrac{P_{i,j}^{n-1/2}\hat{\varepsilon}_{i,j}^{n-1/2}-P_{i-1,j}^{n-1/2}\hat{\varepsilon}_{i-1,j}^{n-1/2}}{\Delta x_{i-1/2}} & if \quad P_{i,j}^{n-1/2}>0\\ \dfrac{P_{i+1,j}^{n-1/2}\hat{\varepsilon}_{i+1,j}^{n-1/2}-P_{i-1,j}^{n-1/2}\hat{\varepsilon}_{i-1,j}^{n-1/2}}{\Delta x_{i-1/2}+\Delta x_{i+1/2}} & if \quad P_{i,j}^{n-1/2}=0\\ \dfrac{P_{i+1,j}^{n-1/2}\hat{\varepsilon}_{i+1,j}^{n-1/2}-P_{i,j}^{n-1/2}\hat{\varepsilon}_{i,j}^{n-1/2}}{\Delta x_{i+1/2}} & if \quad P_{i,j}^{n-1/2}<0\end{cases} \tag{27}$$

The central difference method was applied to discretize the diffusion term $VIS\hat{\varepsilon}X$ (the difference forms of $VIS\hat{\varepsilon}Y$, $VIS\hat{k}X$, and $VIS\hat{k}Y$ are analogous to $VIS\hat{\varepsilon}X$) as follows:

$$VIS\hat{\varepsilon}X=\frac{1}{\Delta x_i}\left\{\left[\left(\nu_k+\frac{\hat{\nu}_t}{\sigma_\varepsilon}\right)\frac{\partial\left(H\hat{\varepsilon}\right)}{\partial x}\right]_{i+1/2,j}^{n-1/2}-\left[\left(\nu_k+\frac{\hat{\nu}_t}{\sigma_\varepsilon}\right)\frac{\partial\left(H\hat{\varepsilon}\right)}{\partial x}\right]_{i-1/2,j}^{n-1/2}\right\}= \tag{28}$$
$$\frac{1}{\Delta x_i}\left[\left(\nu_k+\frac{\left(\hat{\nu}_t\right)_{i+1/2,j}^{n-1/2}}{\sigma_\varepsilon}\right)\frac{H_{i+1,j}^{n-1/2}\hat{\varepsilon}_{i+1,j}^{n-1/2}-H_{i,j}^{n-1/2}\hat{\varepsilon}_{i,j}^{n-1/2}}{\Delta x_{i+1/2}}-\left(\nu_k+\frac{\left(\hat{\nu}_t\right)_{i-1/2,j}^{n-1/2}}{\sigma_\varepsilon}\right)\frac{H_{i,j}^{n-1/2}\hat{\varepsilon}_{i,j}^{n-1/2}-H_{i-1,j}^{n-1/2}\hat{\varepsilon}_{i-1,j}^{n-1/2}}{\Delta x_{i-1/2}}\right]$$

The horizontal velocity-gradient production term P_h can be discretized as:

$$\left(P_h\right)_{i,j}^{n+1/2}=H_{i,j}^{n+1/2}\left(\hat{\nu}_t\right)_{i,j}^{n-1/2}\left[2\left(\frac{U_{i+1/2,j}^{n+1/2}-U_{i-1/2,j}^{n+1/2}}{\Delta x_i}\right)^2+2\left(\frac{V_{i,j+1/2}^{n+1/2}-V_{i,j-1/2}^{n+1/2}}{\Delta y_j}\right)^2+\left(\frac{V_{i+1/2,j}^{n+1/2}-V_{i-1/2,j}^{n+1/2}}{\Delta x_i}+\frac{U_{i,j+1/2}^{n+1/2}-U_{i,j-1/2}^{n+1/2}}{\Delta y_j}\right)^2\right] \tag{29}$$

According to the expression of Eq. (22b), the vertical velocity-gradient production term $P_{\varepsilon V}$ (the difference form of P_{kV} is the same as $P_{\varepsilon V}$) can be discretized as:

$$\left(P_{\varepsilon V}\right)_{i,j}^{n+1/2}=2464.16{C_\mu}^2C_{2\varepsilon}\frac{\left\{\frac{f}{8}\left[\left(U_{i,j}^{n+1/2}\right)^2+\left(V_{i,j}^{n+1/2}\right)^2\right]\right\}^2}{H_{i,j}^{n+1/2}} \tag{30}$$

2.4 Boundary conditions

To perform the staggered-grid difference method, ghost cells are typically imposed around the outmost computational domain. The boundary of all scalar variables, e.g., η^B, $\hat{k}^B$, and $\hat{\varepsilon}^B$ (where the superscript B denotes the boundary) is set at the center of the ghost grid; the boundary of all vector variables, e.g., P^B and Q^B, is located at the center of the adjacent surface between the ghost cell and the outermost computational grid [27]. The boundary conditions selected for this study mainly include open boundaries and no-slip boundaries.

Open boundary conditions are applied mainly to inflow and outflow. For the tests conducted, subcritical flow is the most frequent, hence the boundary conditions assumed include a specific flow rate assigned at the upstream boundary location; in addition, uniform water depth is applied as the downstream boundary condition. The inflow boundary condition can be expressed as follows:

$$\eta_1^{\mathrm{B}} = \eta_2^{\mathrm{B}},\ P_{3/2}^{\mathrm{B}} = P_{5/2}^{\mathrm{B}},\ Q_1^{\mathrm{B}} = Q_2^{\mathrm{B}},\ \hat{k}_1^{\mathrm{B}} = \hat{k}_2^{\mathrm{B}} \text{ and } \hat{\varepsilon}_1^{\mathrm{B}} = \hat{\varepsilon}_2^{\mathrm{B}} \tag{31a}$$

The outflow boundary condition can be expressed follows:

$$\eta_n^{\mathrm{B}} = \eta_{n-1}^{\mathrm{B}},\ P_{n-1/2}^{\mathrm{B}} = P_{n-3/2}^{\mathrm{B}},\ Q_n^{\mathrm{B}} = Q_{n-1}^{\mathrm{B}},\ \hat{k}_n^{\mathrm{B}} = \hat{k}_{n-1}^{\mathrm{B}} \text{ and } \hat{\varepsilon}_n^{\mathrm{B}} = \hat{\varepsilon}_{n-1}^{\mathrm{B}} \tag{31b}$$

No-slip boundary conditions are applied on the side where there is the solid-wall. The flux on the solid boundary is zero, i.e., $P_{l+1/2}^{\mathrm{B}} = Q_{l+1/2}^{\mathrm{B}} = 0$, where the subscript $l+1/2$ denotes the adjacent surface between the water and solid-wall cells and l denotes the corresponding center of the wall cell. The boundary conditions for $\hat{k}$ and $\hat{\varepsilon}$ at the location l are also necessary.

According to the boundary-layer theory, if the distance s between l and $l+1/2$ is sufficiently small, the shear stress and the turbulent production at l can be balanced approximately with the wall shear stress and the dissipation at $l+1/2$, respectively [13]. The depth-averaged statistic characteristics in the small region near the wall are assumed to be analogous to the turbulent features in the core region near the bed. In other words, per Eqs. (8), (11), and (15), $\hat{\varepsilon}_l^{\mathrm{B}}$ can be expressed approximately as follows:

$$\hat{\varepsilon}_l^{\mathrm{B}} = u_{\mathrm{W}*}{}^2 \frac{dU'}{dy'} = \frac{u_{\mathrm{W}*}{}^3}{\kappa s} \tag{32a}$$

where dU'/dy' is the depth-averaged velocity gradient in normal coordinates near the solid wall. Based on the specifications of $\hat{\nu}_t$ and Eq. (4), $(\hat{\nu}_t)_l^{\mathrm{B}}$ can be expressed as $(\hat{\nu}_t)_l^{\mathrm{B}} = \kappa s u_{\mathrm{W}*}$; $\hat{k}_l^{\mathrm{B}}$ can be written as follows:

$$\hat{k}_l^{\mathrm{B}} = \frac{{u_{\mathrm{W}*}}^2}{\sqrt{C_\mu}} \tag{32b}$$

$u_{\mathrm{W}*}$ must satisfy the following equation [24]:

$$\frac{U'}{u_{\mathrm{W}*}} = \begin{cases} \frac{1}{\kappa}\ln\left(\frac{E u_{\mathrm{W}*} y'}{\nu_k}\right) & \text{for hydraulically smooth wall} \\ \frac{1}{\kappa}\ln\left(\frac{30 y'}{k_s}\right) & \text{for hydraulically rough wall} \end{cases} \tag{33}$$

where $E = 0.9$ is the constant; U' is treated as a depth-averaged shear velocity at l; both s and y' are approximated by half of the normal space step at l.

To secure stable numerical results, the Courant-Friedrichs-Lewy (CFL) number Cr was considered as the stability criterion within the proposed model and to enable its incorporation, the following double stability conditions were imposed for Cr as suggested by the literature [24]:

$$\mathrm{Cr}_{\mathrm{flow}} = \Delta t \max\left\{ \max\left[\left(\frac{|P|/H + \sqrt{gH}}{\Delta x} \right)_{i,j} \right], \max\left[\left(\frac{|Q|/H + \sqrt{gH}}{\Delta y} \right)_{i,j} \right] \right\} \le 1 \tag{34a}$$

$$\mathrm{Cr}_{\mathrm{turbulence}} = \Delta t \max\left\{ \max\left[\left(\frac{2\left(\hat{\nu}_t + \nu_k\right)}{\left(\Delta x\right)^2} \right)_{i,j} \right], \max\left[\left(\frac{2\left(\hat{\nu}_t + \nu_k\right)}{\left(\Delta y\right)^2} \right)_{i,j} \right] \right\} \le 1 \tag{34b}$$

where Δt is set as the minimum of the Δt values calculated by using Eqs. (34a) and (34b).

3 Model Validations

To validate the model previously described to quantify complex turbulence, its performance has been verified against experimental turbulent flows obtained under various circumstances: 1) a uniform gravel bed, 2) a $90°$ bend, and 3) a suddenly expanding section. Numerical results were then compared against measured datasets as well as the calculated values from the standard $\hat{k} - \hat{\varepsilon}$ model and other numerical schemes. To distinguish among the different models' results, "*PF*" and "*RRF*" are used to represent the model constructed by the proposed formula and by Rastogi and Rodi's formula, respectively.

3.1 Turbulent flow in a straight channel with gravel bed

To verify the accuracy of the proposed model in replicating bed roughness and Reynolds number effects on the formation of turbulent features, a series of experiments on open-channel flows over rough beds conducted by Wang et al [38], were used for comparison. The

394 experiments were conducted in a straight flat glass flume 13.5 m long, 0.60 m wide, and 0.60
395 deep [38]. The roughness elements on the bottom of the flume were composed of gravel with
396 median diameter d_{50} ranging from 2 to 40 mm. Throughout all measurements, the simultaneous
397 high-frequency velocities in the middle of the flume were obtained with an acoustic Doppler
398 velocimeter (ADV).
399
400 According to the ensemble averages terms used in this study, velocity samples were gathered
401 to determine the mean flows and turbulent fields in the system. The mean velocities in *x*-, *y*-,
402 and *z*-directions were estimated as follows [24]:

403 $$\overline{u} = \frac{1}{N}\sum_{i=1}^{N} u_i, \overline{v} = \frac{1}{N}\sum_{i=1}^{N} v_i, \overline{w} = \frac{1}{N}\sum_{i=1}^{N} w_i \tag{35}$$

404 where N is the number of samples. The root-mean-square (marked as r.m.s) values of the
405 velocity fluctuations are defined by the sample standard deviation:

406 $$\text{r.m.s. } u' = \sqrt{\frac{\sum_{i=1}^{N} u_i^{\,2} - N\overline{u}^{\,2}}{N-1}}, \text{r.m.s. } v' = \sqrt{\frac{\sum_{i=1}^{N} v_i^{\,2} - N\overline{v}^{\,2}}{N-1}}, \text{r.m.s. } w' = \sqrt{\frac{\sum_{i=1}^{N} w_i^{\,2} - N\overline{w}^{\,2}}{N-1}} \tag{36}$$

407 The turbulent kinetic energy k can be calculated from the above definitions as follows:

408 $$k = \frac{1}{2}\left[(\text{r.m.s. } u')^2 + (\text{r.m.s. } v')^2 + (\text{r.m.s. } w')^2\right] \tag{37}$$

409
410 The corresponding depth-averaged $\hat{k}$ can be obtained by depth-averaging the vertical profiles.
411 The depth-averaged data calculated from vertical measured regions was taken to represent the
412 entire depth at the corresponding horizontal coordinate due to the operation constraints of the
413 ADV. The deviations between the depth-averaged velocities obtained by this method and those
414 calculated by the logarithm profile in whole depth are around 5% [24].
415
416 The calculating dimensions in the numerical experiments were $4.0\text{ m} \times 0.6\text{ m} \times 0.6\text{ m}$, which
417 are consistent with the turbulent regime used by Wang et al. [38]. The roughness heights of the
418 glass wall and the gravel bed were set to $k_s = 0.02$ mm and $k_s = d_{50}$, respectively [39]. k_s is the
419 same in the glass bed as the wall. A uniform grid size $\Delta x = \Delta y = 0.02$ m and time step of
420 0.002 s were used in the computation. Eleven typical cases of different gravel d_{50} and Reynolds
421 numbers (Table 1) were analyzed. Considering the weight balance between the boundary
422 conditions and fully turbulent development in regards to the effects of the turbulent structure in

423 the numerical flume, the inflow unit volume flux and outflow water depth were set to H_0U_0 and
424 H_0, respectively.
425
426 According to the measurement results, $\hat{k}$ was strongly dependent on the flow conditions when
427 k_s was constant and it increased as *Re* increased. It is demanding to make any definite
428 conclusion regarding the effects of k_s on $\hat{k}$, however, because it is too difficult to keep *Re* or
429 *Fr* neatly constant in any experiment. The ADV operation limitations and geometrical
430 inhomogeneity over the gravel bed were likely to be responsible for this phenomenon.
431
432 The numerical results of the models derived from different expressions of P_{kV} and $P_{\varepsilon V}$ are also
433 presented in Table 1. The *PF* values deviate slightly from the measured data, but there is
434 reasonable agreement between them for the given ranges of k_s and *Re*. The *RRF* results
435 contained larger error than PF considering the whole range of results. The average of the error
436 for all the test cases C1 to C11, for the *PF* and *RRF* models are, respectively, 49.67 and
437 108.45%. With low bed roughness, $k_s < 5\,\text{mm}$, both sets of results deviate gradually from the
438 experimental values as k_s decreases. This behaviour can be attributed to the anisotropic
439 tendency under which turbulent energy is redistributed over a smooth bed more slowly than
440 over a rough one, which may be enhanced as roughness size decreases. Overall, the results
441 show that the proposed model can effectively simulate turbulent flows over most of the gravel
442 bed.

443 ***3.2 Turbulence of open-channel flow in a $90°$ bend***

444 Furthermore, the performance of numerical models *PF* and *RRF and* other models presented
445 by Cea et al. [11] was compared against turbulent flows in open channel with a $90°$ bend based
446 on the experimental conditions described by Bonillo [40]. The experimental setup was identical
447 to that described by Cea et al. [11], as shown in Fig. 3. The flow domain was made of two
448 straight flat sections linked by a $90°$ bend. The length and width of the first section were 4.835
449 m and 0.86 m, respectively; those of the second section were 4.43 m and 0.72 m, respectively.
450 The bed of Segment 1 is 0.013 m higher than the bottom of Segment 2. The bottom and two
451 sidewalls of the open channel are made of smooth concrete.
452
453 For calculation convenience and comparability among similar models, the flow region was
454 discretized using a uniform grid of $\Delta x = \Delta y = 0.02\text{m}$. The Manning's coefficient of the bed
455 surface selected was the same as Cea et al.'s [11] $0.016\,\text{s}/\text{m}^{1/3}$. The roughness height of the

sidewall surface was assumed to be $k_s = 0.001\text{m}$ [39]. The time step was fixed to $\Delta t = 0.005\,\text{s}$ to maintain numerical stability. The resulting $\hat{k}$ values at three different cross sections are shown in Fig. 4. The values calculated by two classical turbulence models [11], the *KE* model and *RSM* model, are also included. Cea et al. [11] also developed a finite volume model to solve 2D SWEs, in which two famous turbulence models were used for comparison. The KE model is based on the assumption of isotropic eddy viscosity to solve the Reynolds stresses, while the RSM model directly solves each Reynolds stress without any restrictive hypothesis. Though the KE model equations are very similar to those of the RRF model, the location of H in the diffusion term and the value of σ_ε in the former differ from those of the latter.

As shown in Fig. 4, the PF results are very close to the experimental data in both the left sidewall area ($0 \le x \le 4.955$) and right sidewall region ($5.195 \le x \le 5.555$), where B is the width of the channel. There are varying degrees of deviation in the numerical curves of the other three models. In short, the flow features in both regions can be captured adequately by the PF model. In the intermediate region ($4.955 \le x \le 5.195$), none of the numerical curves matched the measured data. This may be because the basic assumption of the shallow water equations is difficult to satisfy in the strong shear and bend zone, which includes intense 3D turbulence. The proposed model yielded accurate results overall despite some data scattering in the shear region.

3.3 Turbulent characteristics in an expanding section

An additional experiment was conducted to determine whether the proposed model can simulate the turbulent flows on an expanding channel [24]. The experiment was carried out in a flat expanding flume at the Hydraulic Engineering Laboratory at National University of Singapore. The length, width, and depth of the flume are respectively 15 m, 0.6 m, and 0.6 m. As shown in Fig. 5, the widths of the channel upstream and downstream of $x = 0$ are 0.3 m and 0.6 m, respectively. The steady flows were strictly controlled by two pumps and a tail gate during the experiment; boundary conditions were the discharge at upstream (0.024 m^3/s) and the flow depth at downstream (0.015 m), respectively. 137 regular points of the intersection were set between the longitudinal coordinates x = -0.10, 0.25, 0.50, 0.75,1.00, 1.25, 1.50, 1.75, 2.00, 2.25, 2.50, 2.75, and 3.00 m and the lateral coordinates y = 0.05, 0.10, 0.15, 0.20, 0.25, 0.30, 0.35, 0.40, 0.45, 0.50, and 0.55 m to observe velocity profiles and further inspect turbulence changes.

The three-dimensional flow velocities were measured with a SonTek/YSI 16-MHz MicroADV with the sampling rate of 50Hz and the outputs of SNR and correlation factor from the

instrument were monitored following procedure already published in literature [24]. Similar to the process in Section 3.1, the depth-averaged data (U, V, $\hat{k}$, and $\hat{\varepsilon}$) were further obtained.

We used identical numerical settings and discretization as Lin [24] to simulate turbulent flows in this study. The computational analysis was performed in a rectangular region of $9.0\ \text{m} \times 0.6\ \text{m}$ and differentiated by a 180x30 uniform grid with increments of $\Delta x = 0.05$ m and $\Delta y = 0.02$ m; the length and width of the narrow channel upstream were 2.0 m and 0.3 m, respectively. The upstream and downstream boundary conditions were unit volume flux of $0.08\ \text{m}^2/\text{s}$ and water depth of 0.15 m, respectively. The Manning coefficient of the bed was $m = 0.01\ \text{s}/\text{m}^{1/3}$ and the sidewall was considered to be smooth. The time step used was $\Delta t = 0.001$ s.

The computed longitudinal velocities at different transverse sections were non-dimensionalized by the approach velocity U_0 and compared against the experimental results as shown in Fig. 6. In the upstream region without extension, i.e., X_a=-0.1 m, the *U*-velocity distribution was highly uniform. The sudden expansion in the profile of the sidewall induces strong non-uniformity to the velocity profiles, which was clearly observable per the flow separation and wake region in the detached flow. A recirculation zone (i.e., $0 \le x/B \le 8$), which was generated mainly due to the stagnant effect of the right sidewall of the building and the southern boundary of the channel, could also be clearly seen. In the downstream section, the longitudinal velocities gradually tended towards uniformity. By contrast, the maximum forward and backward velocities for both methods closely matched experimental data after the change in channel width, especially in the circulation region.

Similar to the *U*-velocity profiles, the non-dimensional transversal velocities calculated by the two models are shown in Fig. 7. In the main flow region (the area between y = 0.3 and 0.6 m), the computed results agree fairly well with experimental data. A steep velocity gradient occurred downstream of the building due to the strongly deflected flow. In the circulation zone (from y = 0.0 to 0.3 m), the velocity changes computed via *RRF* method do not agree very well with the experimental data. The proposed method agrees slightly better with the experimental data but still underestimates the actual velocity by an average of about 50%. In that region, the distribution of horizontal velocities is quite skewed over the full depth. The improved turbulence model does not sufficiently offset the defect of the hydrodynamic assumption in the deflected zone.

Figure 8 shows a comparison among computed $\hat{k}/U_0^2$ values and experimental data. The proposed method yielded close agreement in the transverse section located X_a=-0.1 m upstream of the abrupt extension, in which the statistical turbulence features are similar to the turbulent characteristics in the open-channel uniform flow. The RRF results, by contrast, overestimated by about 10%. At the upper-right corner of the building, where the flow separation began, sizable boundary irregularities were a source of turbulent energy in the horizontal direction. The horizontal bursts of turbulent activity propagated downstream and expanded on both sides, forcing the $\hat{k}$ values towards uniformity. Despite some scattering in the circulation zone, *PF* yielded slightly more accurate results than *RRF* overall.

The dimensionless profiles of turbulent dissipation $\hat{\varepsilon}$ calculated by the two models were compared against experiment data as shown in Fig. 9. In the main area and circulation zone, the *PF* results were a better fit to the data than the *RRF* results. In the transitional region between them, especially near the corner of the building, high levels of energy dissipation were produced due to large-scale eddies and a steep velocity gradient. The proposed method better reflected this phenomenon than the *RRF*, but still overestimated it by around 80%. The difference is mainly attributable to experimental error due to ADV operation limitations and partly by the strong 3D flow structure in corresponding regions. These results altogether indicate that *PF* can better describe the hydraulic and turbulent structure in the abrupt expanding channel than *RRF*.

4 Turbulent Flows near Two Groins in a Natural Waterway

To further investigate the performance of the model developed and illustrate its engineering application, it was used to compute complex turbulent flows and the correspondent navigation conditions in natural waterways and waterways after the construction of two buildings.

4.1 Site description and numerical setup

The Yangliu moraine is located in a relatively straight gorge on the upper reach of the Yangtze River, approximately 1017.8 km upstream of Yichang City, a prefecture-level city in Hubei Province, China. The length and width of the moraine are respectively 1800 m and 400 m, as shown in Fig. 10. The top level of the moraine near the mid-channel, where the highest point is 5 m above the designed water level, is higher than the shoreline. To this effect, the unique bed structure forms a concave basin. The water level in the river must be at least 1 m higher than the designed level to satisfy the necessary flow conditions. Under the restriction of the moraine, the main channel was squeezed to only 250 m in width. Another upstream moraine section of the main reach, the Huangjia moraine, is affected by a shorter lateral flow area with 300 m. A

558 transitional shallow zone (width 500 m) was formed between the two moraines.
559
560 The transitional region, in which the flow is relatively slow, has a flat and straight geometric
561 bed. There is no erosion of river bed material along the ship route during the dry seasons due
562 to hydrodynamic limitations, hence there is only a small water depth for navigation during this
563 period. The minimum depths were recorded in 1993 and 2006, 2.3 m and 2.5 m, respectively.
564 Under these hydraulic conditions, it is very challenging to satisfy the class Ⅲ navigation
565 conditions necessary for free travel of ships with dimensions $560\,\mathrm{m} \times 50\,\mathrm{m} \times 2.7\,\mathrm{m}$.
566
567 To guarantee class Ⅲ navigational standards throughout the entire year, the local waterway
568 bureau constructed two groins on the left side of the shallow region in 2008 (Fig. 10). Groin 1
569 was built at the upstream reach with a $60°$ angle between its axis and the main stream for
570 smooth flow transition. Groin 2 was constructed at the downstream end with a corresponding
571 angle of $75°$. The length of the two groins are respectively 281 m and 313 m; both of their
572 hook heads are 87 m.
573
574 The local waterway bureau measured the bed topography of the reach, the water surface
575 elevation on the shipping route, and the flow velocity in three streamlines on January 15th, 2010,
576 to investigate the effects of the two groins on the waterway (Fig. 10) and the consequent
577 riverbed erosion. For this specific date, the total discharge recorded at the upstream section was
578 3120 m^3/s and the average water level at the downstream section was 253.44 m, values derived
579 by a nearby hydrological station and a water gauge, respectively.
580
581 According to the geological analysis conducted to characterise the properties of the soil in the
582 two boreholes (N1 and N2, as shown in Fig. 10), the bed materials of the transitional shoal
583 region are mainly composed of boulders, sand-cobbles, and brick red sandstones. The mixture
584 of boulders and sand-cobbles typically forms a covering layer 2.3 m thick above the base layer
585 composed by sandstones. The maximum boulder particle-size is 0.9 m and the mass percentage
586 of sand-cobble with 0.03-0.2 m diameter is about 65%. The sieving results at N1 and N2
587 indicate that d_{50} in the reach is approximately 0.04 m.
588
589 The river section that was simulated within the model developed to verify its applicability is
590 1964 m long and 924 m wide, based on the topographic features of Yangliu and Huangjia
591 moraines (Fig. 10). The region that was computed was discretized by applying a uniform
592 Cartesian grid size with dimensions $\Delta x = \Delta y = 4$ m. The median particle size of the bed

material was set at d_{50} = 0.04 m and the time step was set at $\Delta t = 0.002$ s. A flow rate of 3120 m^3/s and an averaged water surface elevation of 253.44 m were respectively assigned to the inflow and outflow boundaries according to the simplified methods presented by Zhang [41].

4.2 Results and performance

Figure 11 shows the comparisons between observed and simulated water levels along the ship route. The average discrepancy between observed data and *PF* results is 0.124 m, while the discrepancy between observed data and *RRF* results is 0.127 m. Although *PF* slightly outperforms *RRF*, especially in the transition section, both have discrepancies from the measured data. This is mainly due to the uniform roughness coefficient that was imposed in the whole river, which does not replicate accurately the natural variety of roughness along the system. In fact, the bed material is uneven in both longitudinal and transverse directions and the bed structure is irregular in such a natural channel hence the bed resistance status could not be characterised by a uniform median size as assumed in this study. Therefore, there is huge potential to greatly improve the results if d_{50} was obtained at each specific site for the numerical calculations.

The flow velocity along three different streamlines was computed and compared against the measured values as shown in Fig. 12. Overall, the calculated curves agree well with the experimental data except in the transition region of Streamline 2, where the maximum absolute deviation was about 0.3 m/s. Similar to the measured water surface elevations, the surveyed points of Streamline 2 were mainly distributed on the route. The d_{50} in the transitional area was generally underestimated. Although there were no significant differences between the two numerical results at most points, *PF* was more accurate than *RRF* near the two groins (the groins are approximately at x = 900 and x = 1200 m, *PF* model is more accurate between x ~ 800-1300 m). Because the turbulence parameters were not measured, we only depict the numerical $\hat{k}$ at two cross sections symbolically to reflect the relevant turbulence characteristics (Fig. 13). The two sections, A-A and B-B (displayed as dash lines in Fig. 10 and their results presented in Fig. 13), are located downstream of the two groins where the longitudinal distance to the root of the groin is approximately equal to the length of the corresponding groin (Fig. 10). As shown in Fig. 13, the numerical values of *RRF* are about 2 times the *PF* results in the mainstream area and approximately 1.5 times *PF*'s in the circulation zone behind the groin. Furthermore, for each method, the numerical values at B-B were larger than those at A-A.

To further explore the navigation scenario discussed above, we calculated the water depth by the proposed model as shown in Fig. 14. In the transitional region of a straight waterway, the

water depth was at least 3.5 m and the width of the water surface was greater than 80 m. To this effect, the river would satisfy category III navigation conditions during the dry season. Our results altogether showed that flow behavior in a natural river can indeed be captured with a reasonable accuracy by the proposed method.

5 Conclusions

This study focused on developing a second-order numerical scheme of spatial staggered-grid difference and temporal leap-frog discretization for simulating the turbulent flows on a complex roughness bed. The model is based on the 2D SWE model and the $\hat{k}-\hat{\varepsilon}$ turbulent closure model. The depth-averaged vertical turbulent generation from the universal notions of the Kolmogorov -5/3 spectrum and the log-law was derived and used as a substitute for the vertical velocity gradient term of the standard $\hat{k}-\hat{\varepsilon}$ model. The proposed $\hat{k}-\hat{\varepsilon}$ model reflects the vertical turbulent production of various scales more robustly than the standard model.

Extensive comparisons were conducted against complex turbulent flows between the proposed model, standard $\hat{k}-\hat{\varepsilon}$ model, and measurement data. The proposed method effectively captured the experimental hydrodynamic features, especially the turbulence characteristics, and improved the simulation accuracy over the standard $\hat{k}-\hat{\varepsilon}$ model. The proposed model also showed better global performance than other 2D shallow numerical schemes.

Furthermore, the turbulent flows over the roughness bed in a natural river were simulated and analyzed. Results showed that the depth-averaged turbulent energy increases as Reynolds number increases when the roughness height is constant. Additionally, the numerical results for Yangliu moraines reach showed that the river navigation conditions are satisfied after constructing the two groins under the flow conditions we considered.

3D simulations will even more adequately disclose the fundamental physics of flows. In this present model application, a large flow domain (Yangliu moraines reach) was considered hence fully 3D computations would have not been very cost-effective. By using the proposed 2D Shallow Water Equations with improved turbulence modelling techniques, it was possible to achieve reasonably engineering accuracy but with a much lower CPU cost. Despite that, considering that 3D analysis would provide a more accurate predictive tool for the flow problems and promote a deeper understanding of the physics of the fluid motion, future work will target the development of an enhanced quasi-three-dimensional shallow flow solver.

Per the large amplitude and gradient of turbulent energy near the structures, local scouring may occur in rainy seasons and gradually alter the bottom configuration, affecting the stability of the groins. To safeguard the regulation buildings, an effective sediment transportation model is necessary to investigate the bed deformation and future research should incorporate more cases to replicate accurately a variety of scenarios to achieve a universal model that can be reliable for each situation.

Acknowledgements

Dr. Xiekang Wang and Dr. Xianye Wang kindly provided the 3D experimental data in Section 3.1. The authors are also grateful to Dr. Luis Cea for the data in Section 3.2.

Funding

This work was supported by the National Key Research and Development Program of China (Grant No: 2016YFE0122500, 2013CB036401 and 2013CB036402), China Postdoctoral Science Foundation (Grant No: 2016M591184) and Programme of Introducing Talents of Discipline to Universities (Grant No: BC2018038).

Notation

f = bed friction factor (-)

g = gravitational acceleration (ms^{-2})

H = water depth (m)

k = turbulent energy (m^2s^{-2})

$\hat{k}$ = depth-averaged turbulent energy (m^2s^{-2})

k_s = equivalent sand roughness (m)

l_m = length scale of turbulent flow (m)

m = Manning's roughness coefficient ($sm^{-1/3}$)

P,Q = unit volume flux in x- and y-directions, respectively (m^2s^{-1})

R = hydraulic radius (m)

Re = Reynolds number (-)

T_{xx}, T_{yy} = depth-averaged normal stress in x- and y-directions, respectively (Pa)

T_{yx}, T_{xy} = depth-averaged shear stress in x- and y-directions, respectively (Pa)

u^* = velocity scale of turbulent flow (ms^{-1})

u_* = friction velocity (ms^{-1})

U, V, W = depth-averaged velocity in x-, y- and z-directions, respectively (ms^{-1})

693 u, v, w = instantaneous velocity in x-, y- and z-directions, respectively (ms^{-1})

694 $\overline{u}, \overline{v}, \overline{w}$ = ensemble-averaged velocity in x-, y- and z-directions, respectively (ms^{-1})

695 u', v', w' = fluctuating velocity in x-, y- and z-directions, respectively (ms^{-1})

696 $\langle u \rangle, \langle v \rangle, \langle w \rangle$ = mean velocity in x-, y- and z-directions, respectively (ms^{-1})

697 $\|u'\|, \|v'\|, \|w'\|$ = turbulence intensity in x-, y- and z-directions, respectively (ms^{-1})

698 x, y, z = streamwise, spanwise, and vertical coordinates, respectively (-)

699 z_b = bed elevation (m)

700 ε = turbulent dissipation (m^2s^{-3})

701 $\hat{\varepsilon}$ = depth-averaged turbulent dissipation (m^2s^{-3})

702 η = free surface elevation (m)

703 ν = turbulent viscosity (m^2s^{-1})

704 ν_k = kinematic viscosity (m^2s^{-1})

705 $\hat{\nu}_t$ = depth-averaged turbulent viscosity (m^2s^{-1})

706 ρ = fluid density (kgm^{-3})

707 τ = total shear stress (Pa)

708 τ_b = bed shear stress (Pa)

709

710 **References**

711 1. Rodi, W., Mansour, N. N. (1993), Low Reynolds number $k-\varepsilon$ modelling with the aid of
712 direct simulation data, J Fluid Mech 250, 509-529.

713 2. Pope, S. B. (2000), Turbulent Flows, Abingdon, Routledge.

714 3. Bhaganagar, K., Kim, J., Coleman, G. (2004), Effect of roughness on wall-bounded
715 turbulence, Flow, Turbulence and Combustion, 72, 463–492.

716 4. Hinterberger, C., Fröhlich, J., Rodi, W. (2008), 2D and 3D turbulent fluctuations in open
717 channel flow with $\mathrm{Re}_\tau = 590$ studied by large eddy simulation, Flow, Turbulence and
718 Combustion, 80, 225–253.

719 5. Erpicum, S., Meile, T., Dewals, T. M., Pirotton, M., Schleiss, A. J. (2009), 2D numerical
720 flow modeling in a macro-rough channel, Int J Numer Meth Fluids, 61, 1227–1246.

721 6. Younus, M., Chaudhry, M. H. (1994), A depth-averaged $\hat{k}-\hat{\varepsilon}$ turbulence model for the
722 computation of free-surface flow, Journal of Hydraulic Research, 32(3), 415-444.

723 7. Cao, Z. X., Hu, P. H., Hu, K. H., Pender, G., Liu, Q. H. (2014), Modelling roll waves with
724 shallow water equations and turbulent closure, Journal of Hydraulic Research, 53(2), 161-
725 177.

8. Pu, J. H., Shao, S. D., Huang, Y. F. (2014), Numerical and experimental turbulence studies on shallow open channel flows, Journal of Hydro-environment Research, 8, 9-19.
9. Campomaggiore, F., Cristo, C. D., Iervolino, M., Vacca, A. (2016), Inlet effects on roll-wave development in shallow turbulent open-channel flows, J Hydrol Hydromech, 64(1), 45-55.
10. Duan, J. G. (2004), Simulation of flow and mass dispersion in meandering channels, Journal of Hydraulic Engineering, 130(10), 964–976.
11. Cea, L., Puertas, J., Gázquez-Cendón, M. E. (2007), Depth averaged modelling of turbulent shallow water flow with wet-dry fronts, Arch Comput Methods Eng, 14, 303-341.
12. Rastogi, A. K., Rodi, W. (1978), Predictions of heat and mass transfer in open channels, J Hydr Div, 104(3), 397-420.
13. Launder, B. E., Spalding, D. B. (1974), The numerical computation of turbulent flows, Computer Methods in Applied Mechanics and Engineering, 3, 269-289.
14. Wu, W. M., Wang, P. Y., Chiba, N. (2004), Comparison of five depth-averaged 2-D turbulence models for river flows, Archives of Hydro-Engineering and Environmental Mechanics, 51(2), 183-200.
15. Chen, Y. S., Kim, S. M. (1987), Computation of turbulent flows using an extended $k-\varepsilon$ turbulence closure model, CR-179204, NASA, pp21.
16. Booij, R. (1989), Depth-averaged $k-\varepsilon$ modelling, In Proc 23rd IAHR Congress, Delft, The Netherlands, Vol A, IAHR, pp. 198–206.
17. Babarutsi, S., Chu, V. H. (1991), A two-length-scale model for quasi two-dimensional turbulent shear flows, In Proc 24th Congress of IAHR, Madrid, Spain, Vol C, IAHR, pp 51–60.
18. Yakhot, V., Orszag, S. A., Thangam, S., Gatski, T. B., Speziale, C. G. (1992), Development of turbulence models for shear flows by a double expansion technique, Phys Fluids A, Fluid Dynamics, 4(9).
19. Richardson, L. F. (1922), Weather Prediction by Numerical Process. Cambridge: Cambridge University Press.
20. Nezu, I., Nakagawa, H. (1993), Turbulence in Open-channel Flows, A. A. Balkema, Rotterdam.
21. Hunt, J. C. R., Eames, I., Westerweel, J., Davidson, P. A., Voropayev, S., Fernando, J., Braza, M. (2010), Thin shear layers - The key to turbulence structure, Journal of Hydro-environment Research, 4, 75-82.
22. Kolmogorov, A. N. (1941), The local structure of turbulence in incompressible viscous fluid for very large Reynolds number, CR Acad Sci URSS, 30, 301-305.

762 23. Cho, Y. S. (1995), Numerical Simulations of Tsunami Propagation and Run-up, PhD
763 dissertation, Cornell University, Ithaca, NY.
764 24. Lin, Q. H. (2009), Numerical Simulation of Sediment Transport and Morphological
765 Evolution, PhD dissertation, National University of Singapore, Singapore.
766 25. Lin, P. Z., Wu, Y. N., Bai, J. L., Lin, Q. H. (2011), A numerical study of dam-break flow
767 and sediment transport from a quake lake, Journal of Earthquake and Tsunami, 5(5), 401-
768 428.
769 26. Zhang, Y. (2015), Study of Numerical Model for Simulating Evolution of Dam-break
770 Flows, PhD dissertation, Sichuan University, China.
771 27. Zhang, Y., Lin, P. Z. (2016), An improved SWE model for simulation of dam-break flows,
772 Proceedings of the Institution Civil Engineers – Water Management, 169(6), 260-274.
773 28. Idelchik, I. E. (1994), Handbook of Hydraulic Resistance, CRC Press, 3rd ed. Boca Raton,
774 USA.
775 29. Abbaspour, A., Kia, S. H. (2014), Numerical investigation of turbulent open channel flow
776 with semi-cylindrical rough beds, Journal of Civil Engineering, 18(7), 2252-2260.
777 30. Pu J. H., Wei J., Huang Y. (2017), Velocity distribution and 3D turbulence characteristic
778 analysis for flow over water-worked rough bed, Water, 9(9), 668; doi:10.3390/w9090668.
779 31. Coles, D. (1956), The law of the wake in the turbulent boundary layer, J Fluid Mech, 1,
780 191-226.
781 32. Pu J. H., Tait S., Guo Y., Huang Y., Hanmaiahgari P. R. (2018), Dominant features in
782 three-dimensional turbulence structure: comparison of non-uniform accelerating and
783 decelerating flows, Environmental Fluid Mechanics, 18(2), pp.395-416.
784 33. Nakagawa, H., Nezu, I., Ueda, H. (1975), Turbulence of open channel flow over smooth
785 and rough beds, Proc of Japan Soc Civil Engrs, 241, 155-168.
786 34. Jobson, H. E., Sayre, W. W. (1970), Vertical transfer in open channel flow, J Fluid Mech,
787 122, 295-314.
788 35. Ueda, H., Moller, R., Komori, S., Mizushina, T. (1977), Eddy diffusivity near the free
789 surface of open channel flow, Int J Heat and Mass Transfer, 20, 1127-1136.
790 36. Hussain, A. K. M. F., Reynolds, W. C. (1975), Measurements in fully developed turbulent
791 channel flow, J Fluids Eng, 97, 568-580.
792 37. Nezu, I., Rodi, W. (1986), Open-channel flow measurements with a laser Doppler
793 anemometer, J Hydraulic Eng, 112, 335-355.
794 38. Wang, X. Y., Yang, Q. Y., Lu, W. Z., Wang, X. K. (2012), Experimental study of near-
795 wall turbulent characteristics in an open-channel with gravel bed using an acoustic Doppler
796 velocimeter, Exp Fluids, 52, 85-94.

797 39. Chanson, H. (2004), The Hydraulics of Open Channel Flow: An Introduction,
798 Butterworth-Heinemann, Oxford, UK.
799 40. Bonillo, J. (2000), Un modelo de transporte de sustancias solubles para flujos trubulentos
800 en lamina libre. Tesis doctoral, Área de Ingeniería Hidráulica, Universidad de A Coruña.
801 41. Zhang, Y. (2011), Numerical Simulation of Flow around Groyne with the Different Pick
802 Angles in the Inland Waterways, Master Thesis, Sichuan University, China.
803
804

805

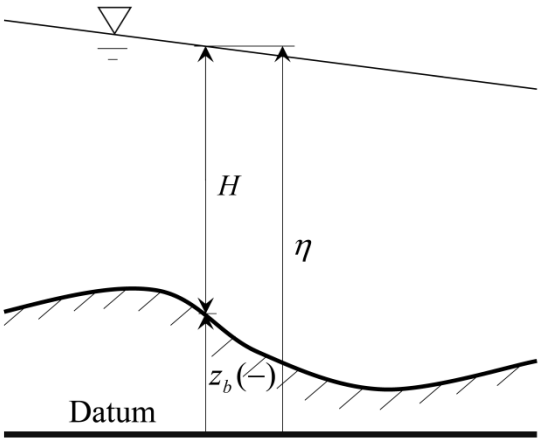

806

807 Figure 1 - Scheme illustrating an example of irregular bed elevation and free surface water
808 depth.

809

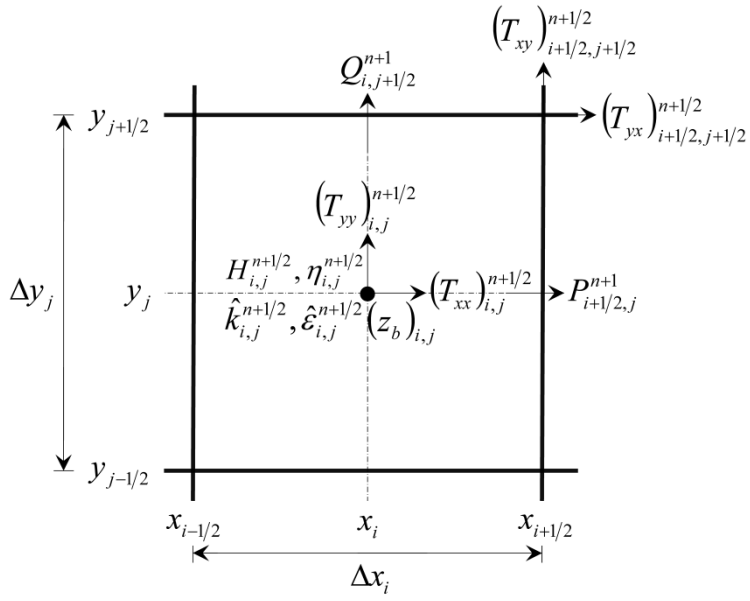

Figure 2 - Scheme of staggered grid which includes the locations of the variables considered in a single cell.

815

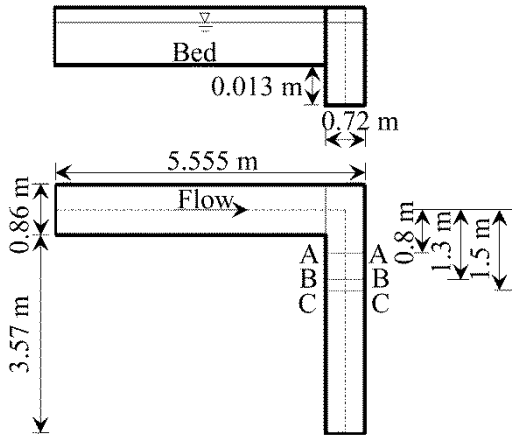

816

817 Figure 3 – Scheme of the experimental channel with a $90°$ bend: front view (top) and top view
818 (bottom).

819

820

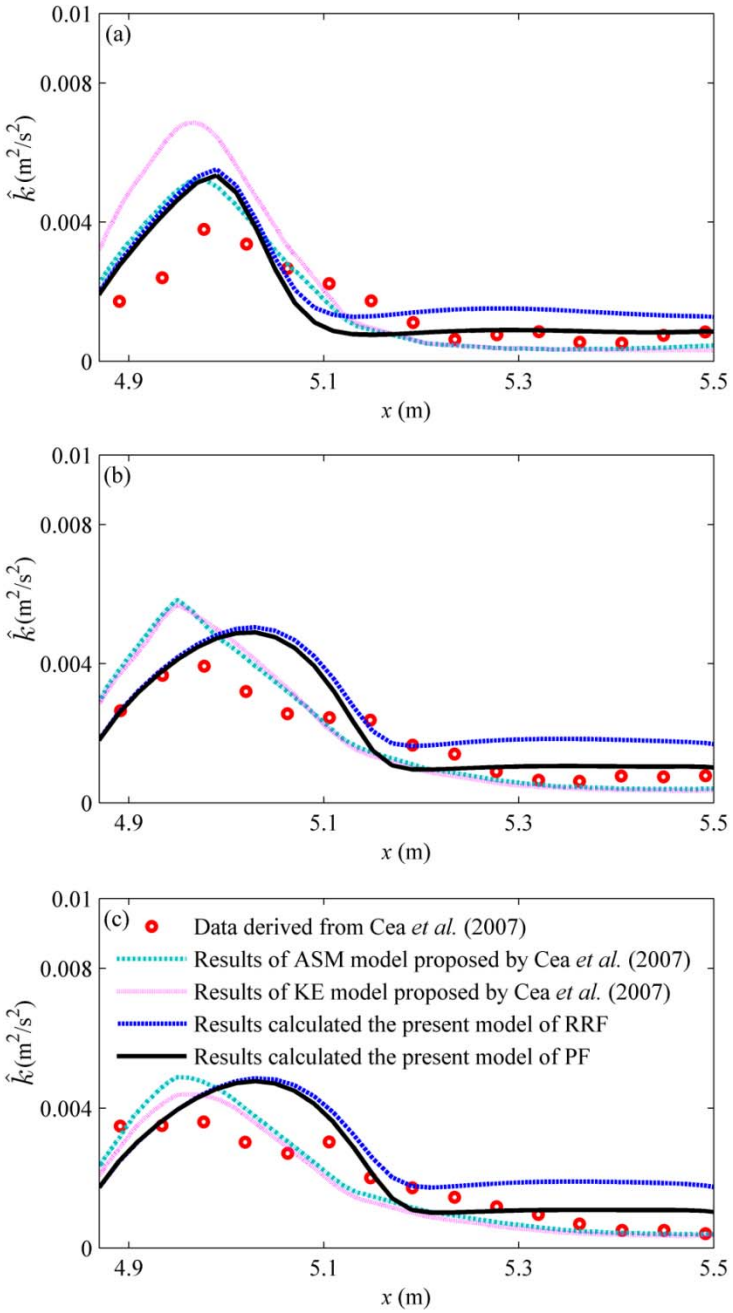

821

822 Figure 4 – Comparison of turbulent kinetic energy measured experimentally and calculated
823 numerically at three sections (a) A-A, (b) B-B and (c) C-C.

824

825

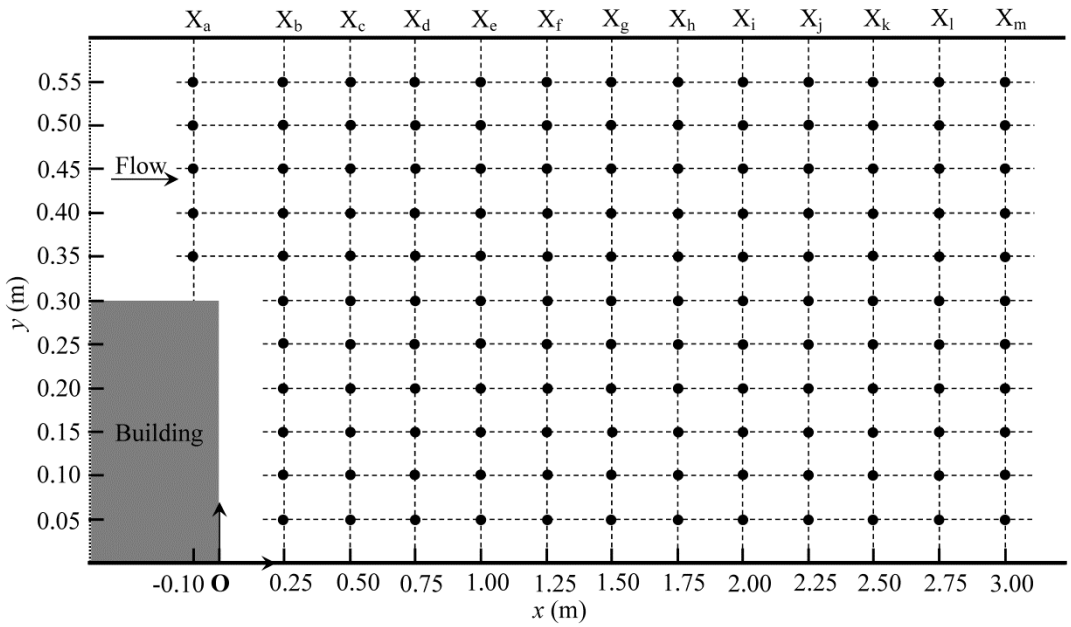

826

827 Figure 5 - Plan view of flume with an expanding section and the observed points.

828

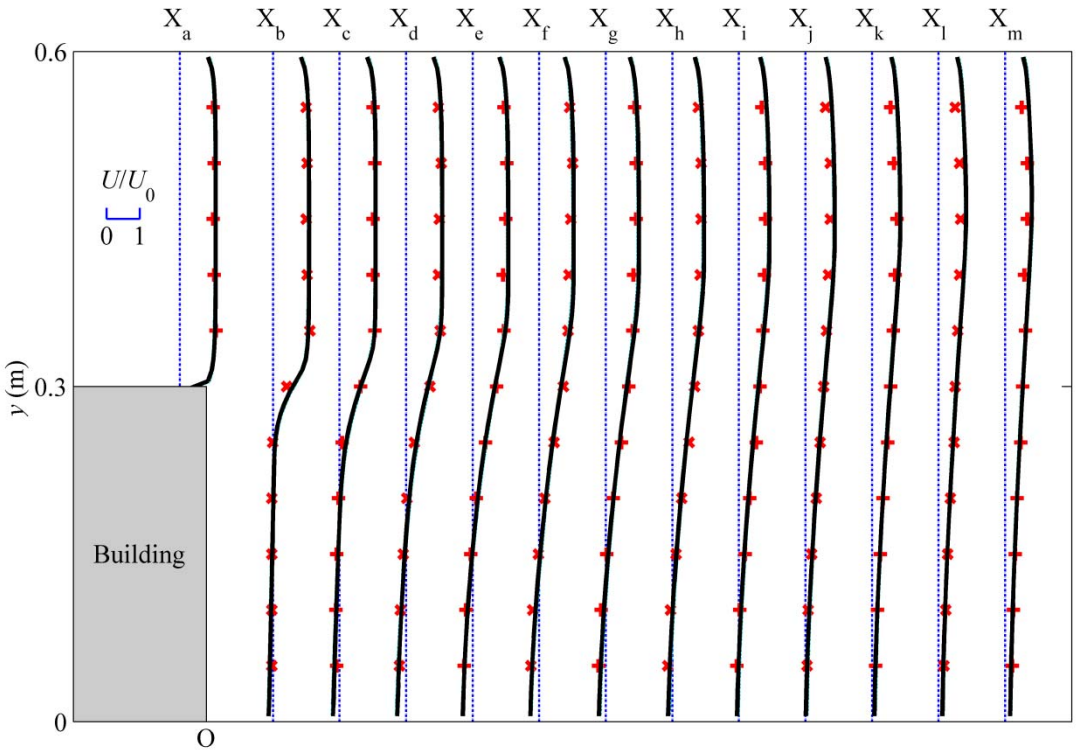

Figure 6 - Comparisons of non-dimensionalized U between numerical results and experimental data (Red crosses: experimental data; Dashed green line: RRF's results; Solid black line: PF's results).

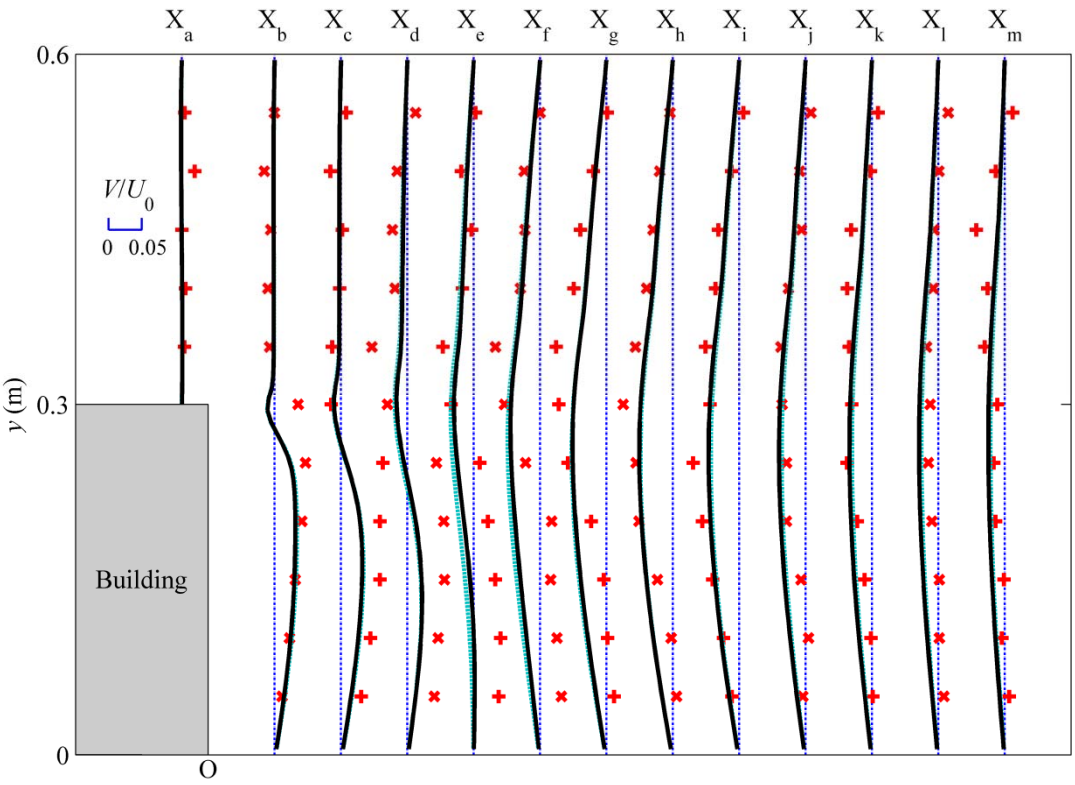

Figure 7 - Comparisons of non-dimensionalized V between numerical results and experimental data (Red crosses: experimental data; Dashed green line: RRF's results; Solid black line: PF's results).

841

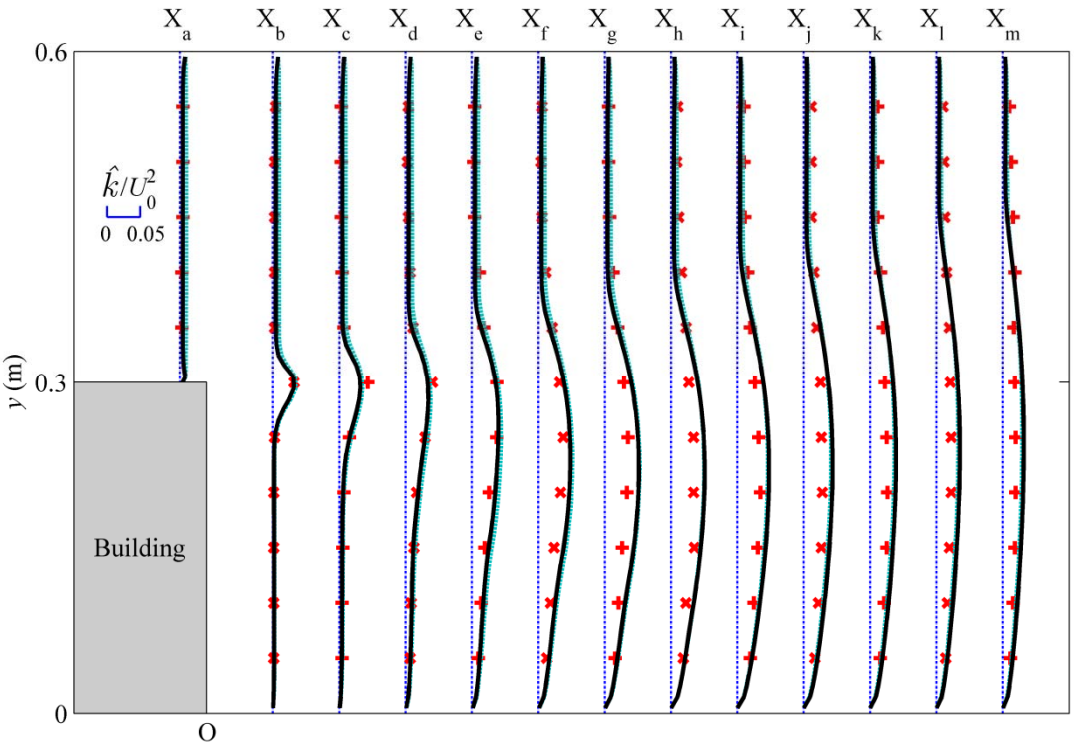

842

843 Figure 8 - Comparisons of non-dimensionalized $\hat{k}$ between numerical results and experimental
844 data (Red crosses: experimental data; Dashed green line: RRF's results; Solid black line: PF's
845 results).

846

847

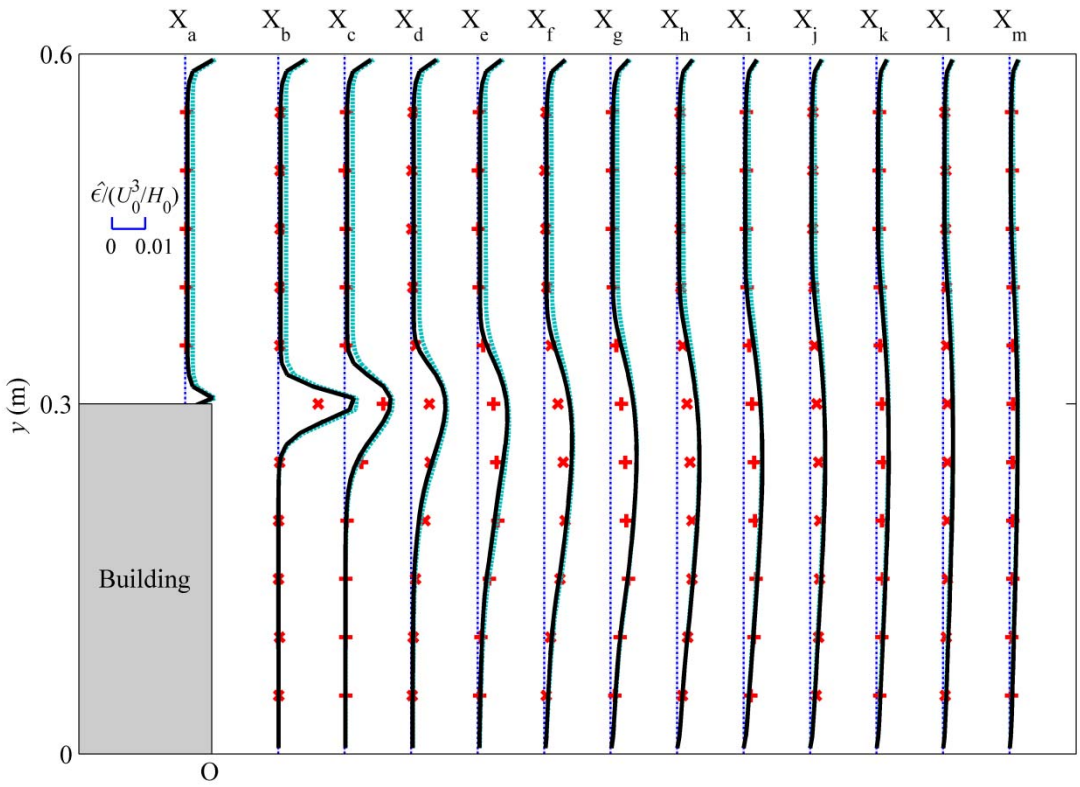

848

849 Figure 9 - Comparisons of non-dimensionalized $\hat{\varepsilon}$ between numerical results and experimental
850 data (Red crosses: experimental data; Dashed green line: RRF's results; Solid black line: PF's
851 results).

852

853

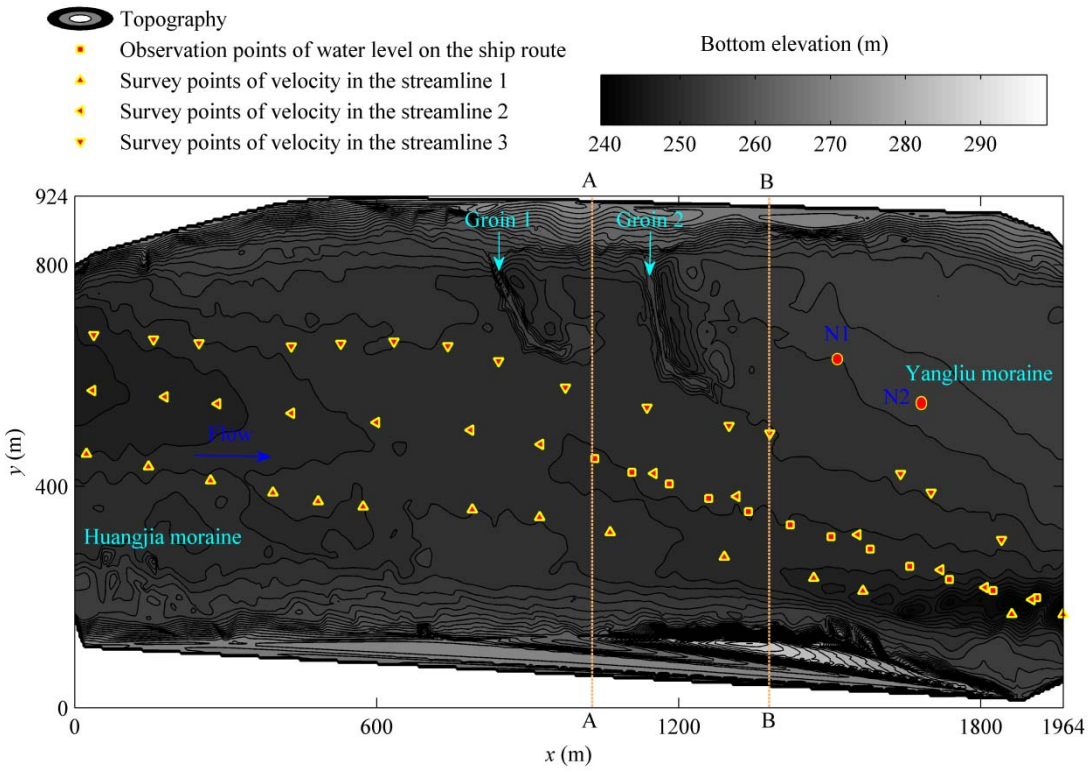

854

855 Figure 10 - Bed topography of Yangliu moraine reach and location of observation points.

856

857

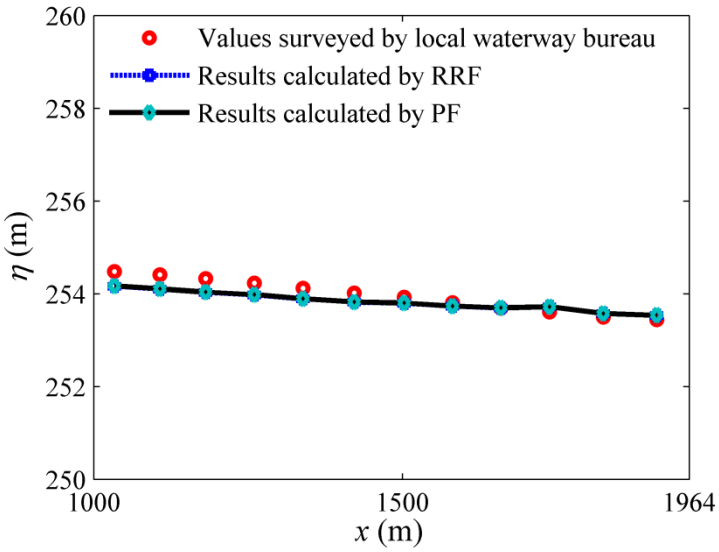

858

859 Figure 11 - Water level comparison between observed data and computed results on the ship
860 route.

861

862

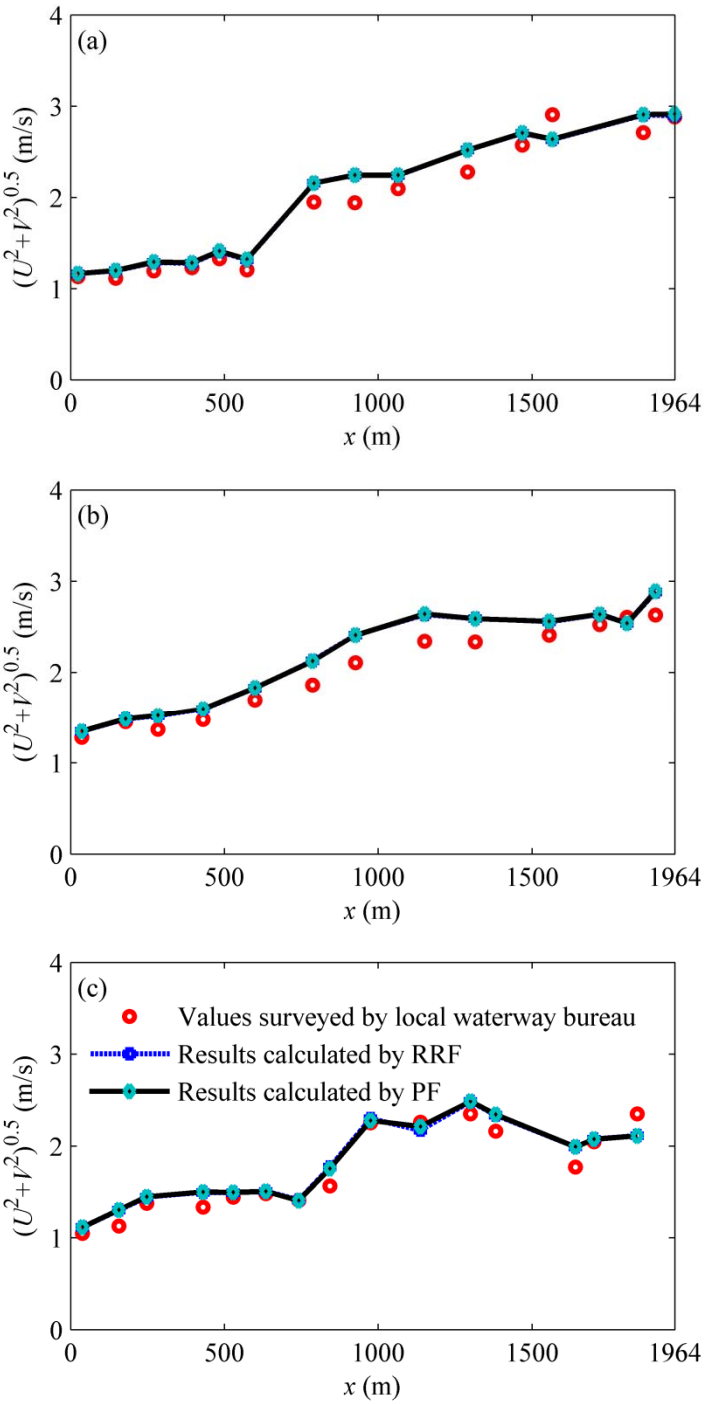

863

864 Figure 12 - Flow velocity comparison between measured values and calculated results in the
865 three streamlines: (a) streamline 1, (b) streamline 2 and (c) streamline 3.

866

867

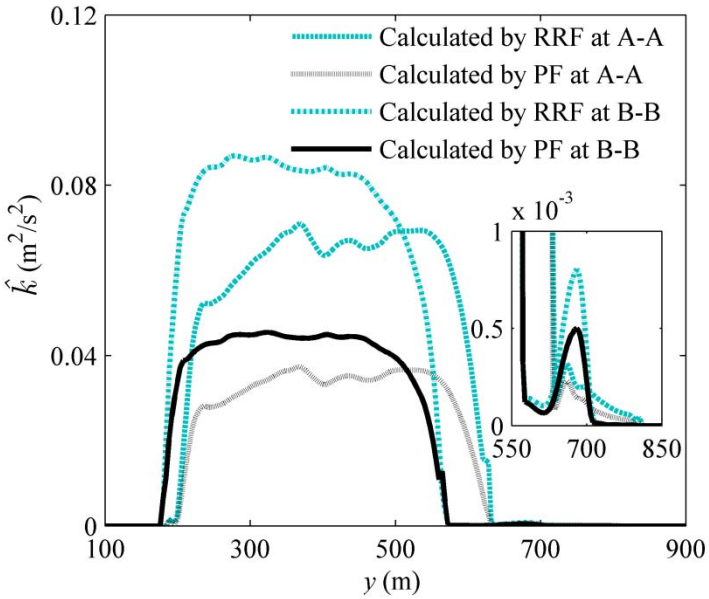

868

869 Figure 13 - Comparisons of the numerical results between PF and RRF at the sections of A-A
870 and B-B behind the two groins.

871

872

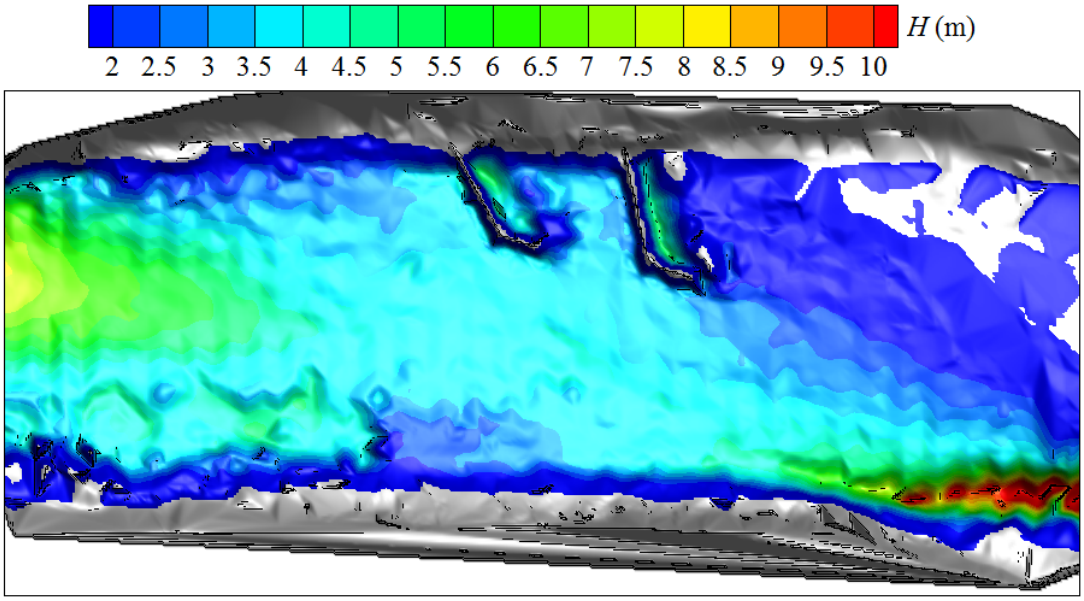

873

874 Figure 14 - Water depth calculated by the proposed model.

875

876

877 Table 1. Hydraulic data collected with the experiments and numerically calculated.

Case	k_s	H	U_0	Re	Fr	$\hat{k}$ acquired from measurements $(\times 10^{-3})$ m^2/s^2	$\hat{k}$ simulated by PF		$\hat{k}$ simulated by RRF	
	mm	cm	cm/s				Results $(\times 10^{-3})$ m^2/s^2	Relative Absolute Error %	Results $(\times 10^{-3})$ m^2/s^2	Relative Absolute Error %
C1	0.02	50.2	34.0	170,680	0.15	2.83	0.33	88.3	0.77	72.8
C2	2	42.0	36.2	152,040	0.18	2.36	0.70	70.3	1.40	40.7
C3	5	24.8	65.3	161,944	0.42	3.41	3.20	6.2	5.83	71.0
C4	10	19.6	46.3	90,748	0.33	1.85	2.04	10.3	3.51	89.7
C5	10	30.7	57.8	177,446	0.33	3.81	2.84	25.5	5.02	31.8
C6	10	19.4	101.0	195,940	0.73	5.27	8.48	60.9	14.69	178.7
C7	20	31.8	42.7	135,786	0.24	2.35	1.84	21.7	3.12	32.8
C8	20	28.1	63.5	178,435	0.38	2.45	4.14	69.0	6.96	184.1
C9	40	28.8	35.4	101,952	0.21	0.89	1.55	74.2	2.49	179.8
C10	40	29.5	62.5	184,375	0.37	3.24	4.70	45.1	7.60	134.6
C11	40	17.5	110.5	193,375	0.84	7.22	12.63	74.9	20.00	177.0

878 k_s: gravel median diameter d_{50}, H and U_0: average vertical distance from gravel bed to
879 water surface and bulk free-stream velocity in the middle section of the experimental flume,
880 respectively.
881